MEASUREMENT OF CEREBRAL BLOOD FLOW USING ARTERIAL SPIN LABELING MAGNETIC RESONANCE IMAGING

APPROVED BY SUPERVISORY COMMITTEE

Hanzhang Lu, Ph.D. _____

Vikram Kodibagkar, Ph.D. _____

Robert Eberhart, Ph.D. _____

Roderick McColl, Ph.D. _____

Hao Huang, Ph.D. _____

DEDICATIONS

To my parents, Elahe and Shapour Aslan, who made much sacrifice in raising me and making a tough decision to send me abroad for a better education and future.

To my uncle, Hessam Aletaha, whose valuable advice guided me during the early stage of my adulthood and laid the foundation for my success in life.

To my beloved wife, Nyaz Didehbani, whose unconditional support and love inspired me throughout my studies and helped me to achieve my goals in life.

To my mentor, Dr. Hanzhang Lu, who taught me how to think scientifically and supported me throughout my doctoral degree.

MEASUREMENT OF CEREBRAL BLOOD FLOW USING ARTERIAL SPIN LABELING MAGNETIC RESONANCE IMAGING

By

SINA ASLAN

DISSERTATION

Presented to the Faculty of the Graduate School of Biomedical Sciences

The University of Texas Southwestern Medical Center at Dallas

In Partial Fulfillment of the Requirements

For the Degree of

DOCTOR OF PHILOSOPHY

The University of Texas Southwestern Medical Center at Dallas

Dallas, Texas

December, 2010

ABSTRACT

MEASUREMENT OF CEREBRAL BLOOD FLOW USING ARTERIAL SPIN LABELING MAGNETIC RESONANCE IMAGING

SINA ASLAN, Ph.D.

The University of Texas Southwestern Medical Center at Dallas, December 2010

Mentor: Hanzhang Lu, Ph.D.

Cerebral Blood Flow (CBF) reflects the amount of blood perfusion in the brain, often defined as ml of blood per 100 gram of brain per minute. CBF is an important measure in understanding brain physiology and pathophysiology. Thus, it is important to establish a robust method suitable for longitudinal and cross-sectional studies of neurovascular and neurodegenerative diseases non-invasively. Pseudo-Continuous Arterial Spin Labeling (pCASL) MRI is a new MRI technique

that is able to detect blood flow changes, non-invasively. The blood flow change detected by pCASL MRI is relative and it is expressed in terms of arbitrary MRI units which does not have any physiological meaning. Thus, quantifying absolute CBF map is of a great interest. In the first part of this study, I quantified absolute CBF (aCBF) map by utilizing phase contrast MRI as a normalization factor. Next, I provided a systematic investigation into the detection power of ASL and the optimal strategies for data analysis. The power of ASL MRI in detecting CBF differences between patient and control subjects is hampered by inter-subject variations in global CBF, which are associated with non-neural factors and may contribute to the noise in the across-group comparison. I found that when normalizing the CBF with whole-brain CBF or CBF in a reference region (termed relative CBF, rCBF), the statistical significance was improved considerably ($p<0.003$). In the last part of this study, the aCBF of ten major brain human fibers were estimated for the first time and the relationship between Fractional Anisotropy (FA) and aCBF was investigated. The inverse association between aCBF and FA suggests that higher myelination restricted the blood flow to the center of the fiber or higher myelination made the conductance of the action potential more efficient. In summary, ASL MRI has become the method of choice for measuring cerebral blood flow and it has a great potential in clinical settings for diagnosis of most neurological disorders before anatomical changes are observed.

TABLE OF CONTENTS

PRIOR PUBLICATIONS

1. **Aslan S**, Xu F, Wang PL, Uh J, Yezhuvath US, van Osch M, Lu H. Estimation of labeling efficiency in pseudo-continuous arterial spin labeling. Magnetic Resonance in Medicine. 2010 Mar;63(3):765-71.

2. **Aslan S** and Lu H. On the sensitivity of ASL MRI in detecting regional differences in cerebral blood flow. Magnetic Resonance Imaging. 2010 Sep;28(7):928-935.

3. Marquez de la Plata CD, Yang FG, Paliotta C, Wang JY, Krishnan K, Bakhadirov K, **Aslan S**, Devous MD, Sr., Moore C, Harper C, McColl R, Cullum CM, Diaz-Arrastia R. Diffusion Tensor Imaging Biomarkers for Diffuse Axonal Injury: Comparison of Three Analytic Methods. Journal of the International Neuropsychological Society. *In Press*.

4. Wang PL, **Aslan S**, Li X, Buhner DM, Briggs RW, Haley RW, and Lu H. Perfusion deficit to cholinergic challenge in veterans with Gulf War Illness. NeuroToxicology. *Submitted*.

5. **Aslan S**, Huang H, Uh J, Guanghua Xiao, Lu H. Estimation of Cerebral Blood Flow of White Matter Fibers in Human Brain. *In Preparation.*

LIST OF FIGURES

LIST OF TABLES

LIST OF APPENDICES

LIST OF ABBREVIATIONS

aCBF – Absolute Cerebral Blood Flow

AC-PC – Anterior Commissure Posterior Commissure

ASL – Arterial Spin Labeling

a.u. – Arbitrary Units

B – Magnetic field strength

BR – Breath Rate

BBB – Blood Brain Barrier

CASL – Continuous Arterial Spin Labeling

CBF – Cerebral Blood Flow

CC – Correlation Coefficient

CO_2 – Carbon Dioxide

dA – Cross Section of the vessel

DMN – Default Mode Network

DSC MRI – Dynamic Susceptibility Contrast Magnetic Resonance Imaging

DTI – Diffusion Tensor Imaging

etCO_2 – End Tidal CO_2

f – Blood Flow

FA – Fractional Anisotropy

fcMRI – functional connectivity MRI

FDG – ^{18}F-flurodeoxyglucose

FDR – False Discovery Rate

FOV – Field of View

Gd – Gadolinium

GM – Gray Matter

HR – Heart Rate

ICA – Internal Carotid Artery

ICV – Intracranial volume

M – Net magnetization of all spins within a spin system

M_0 – the value of equilibrium magnetization

$M_{x,y,z}$ – Net Magnetization of all spins within a spin system in x, y, or z direction

M_b – Magnetization in Brain

M_b^o – Fully Relaxed value of M_b

M_b^{ss} – Magnetization reached after steady state

MNI – Montreal Neurological Institute

MRI – Magnetic Resonance Imaging

PASL – Pulsed Arterial Spin Labeling

pCASL – Pseudo Continuous Arterial Spin Labeling

PC MRI – Phase Contrast MRI

PET – Positron Emission Tomography

rCBF – relative Cerebral Blood Flow

RF – Radio Frequency

SD – Standard Deviation

SPECT – Single Photon Emission Computed Tomography

SpO_2 – Pulse Oximeter Oxygen Saturation

SNR – Signal to Noise Ratio

TE – Echo Time

TR – Repetition time

T_1 – The time constant that describes the recovery of the longitudinal component of magnetization over time

T_2 – The time constant that describes the decay of transverse component of net magnetization over time

T_{1app} – Apparent T1, magnetization decay of blood in relation to blood flow and corrected for blood brain partition coefficient

T_{1a} – T1 of arterial blood

T_{1b} – T1 of brain tissue

T_{1RF} – T1 of the RF

T1W – T1 weighted image

T2W – T2 weighted image

TOF – Time of Flight

w – Delay of duration

WM – White Matter

V_z – Velocity of arterial blood

VA – Vertebral Artery

VBA – Voxel Based Analysis

ρ – Brain density

γ – Gyromagnetic Ratio

δ – Arterial Transit time

λ – Blood brain partition coefficient

α – Labeling Efficiency

BACKGROUND

Cerebral Blood Flow (CBF) reflects the amount of blood perfusion in the brain, often defined as ml of blood per 100 gram of brain per minute (Austin G et al., 1975). The typical CBF value for the whole brain is 60 ml of blood per 100 grams of brain tissue per minute where women typically have higher CBF value than men (Baxter LR, Jr. et al., 1987; Daniel DG et al., 1989; Devous MD, Sr. et al., 1986). CBF is an important measure in understanding brain physiology and pathophysiology (Detre JA and DC Alsop, 1999). Many pathological conditions are associated with abnormal CBF values, including acute stroke (Strandgaard S and OB Paulson, 1992), brain tumor (Leenders KL, 1994), neurodegenerative diseases and epilepsyis (Grubb RL, Jr. et al., 1974). In addition, it could serve as a critical value in the diagnosis and/or monitoring of treatment for many brain diseases. Furthermore, local changes in CBF also provide an important contrast for functional brain imaging. Accurate estimation of CBF is essential for quantitative fMRI and for understanding the BOLD signal mechanism. Thus, it is important to establish a robust method suitable for longitudinal and cross-sectional studies of neurovascular and neurodegenerative diseases non-invasively.

The history of cerebral circulation and the measurement of CBF study dates back to 2500 B.C. Imhotep, physician of King Zoser, the first pharaoh of the third dynasty, noticed the injuries that slaves had sustained during

construction of pyramids and directed his medical attention to trauma. During the examination of a compound skull fracture with a dural tear, the author observed the pulsation of the exposed brain during life. The word "brain" appears seven times in context of head injury in the surviving papyrus, figure 1. The heart and its pumping action were recognized along with vessels and the pulse (Bell BA, 1984).

Figure 1. A transcription from Professor Breasted's translation of the Edwin Smith papyrus. Case 6: Examination of gaping cranial wound "and something therein throbbing and fluttering under thy fingers. Like the weak place of an infant's crown before it becomes whole."

Brain weighs 2% of the body weight and it consumes 25% of the body's energy. This energy is delivered through four major arteries, namely: left/right internal carotid and left/right vertebral arteries. In late 15th century, Leonardo da Vinci (1452 – 1519) first described the vessels of the neck with some accuracy and suggested the compression of these vessels could lead to unconsciousness. Andreas Vesalius (1514 – 1564) drawings of the anatomy of the cerebral circulation show a communication between the carotid artery and the transverse

sinus, figure 2. In April 1616, William Harvey (1578 – 1657) discovered the circulation of the blood and transformed vascular anatomy into physiology.

Figure 2. The vessels of the brain. (From Vesalius A: *De Humani Corporis Fabrica*. Basel, J Oporinus, 1543, libre VII, and Fishman AP, Richards DW: *Circuilation of the Blood*. Men and Ideas. New York, Oxford University Press, 1964.

The first attempt to understand physiological concept of CBF was suggested by Thomas Willis (1621 – 1675), who coined the name "Circle of Willis". He proposed the function of the circle was to mix the blood before distribution to the brain. Many observational experiments were performed such as direct examination of pia mater; however, it was Paul Jensen, in 1904, who gave the first numerical value for CBF in dog and rabbit (125 ml/100 grams of brain/ minute), measured with Hurthle's stromuhr (Bell BA, 1984). The initial CBF determination in humans were carried out by Kety and Schmidt by inhalation of 15% nitrous oxide for 10 minutes and taking blood samples from

jugular venous and peripheral arterial blood during saturation with the gas. Their CBF estimation was based on Fick's principle:

> The amount of indicator taken up by the tissue per unit of time is equal to quantity brought to the tissue by arterial blood minus the quantity carried away in the venous blood.

This dilution principle can be expressed in blood flow measurement: the faster the blood flow, the less oxygen uptake per unit of blood flowing. Kety and Schmidt examined 14 healthy male volunteers and estimated a mean CBF value of 54 ± 12 ml/100 g of brain/minute (Kety SS and CF Schmidt, 1948). In 1961, CBF estimation became even more significant after Sokoloff demonstrated that the regional CBF and functional activity are coupled (Sokoloff L, 1961).

There are several different methods for measuring CBF, most of which are based on Kety's pioneer work on exchange of diffusible gases in the lungs and tissues. He provided the bases for development of most of the methods of regional flow measurement using inert gases as diffusible indicators. His equations form the basis of all clearance, autoradiographic, and computed tomogram techniques (Kety SS, 1951). Various approaches can be used to label the blood for CBF measurement. For human studies, the typical approach is to either use Nuclear Medicine techniques or MRI for such measurements.

Nuclear Medicine Imaging

In the last 60 years, Single Photon Emission Computed Tomography (SPECT) and Positron Emission Tomography (PET) have gained popularity in tissue function *in vivo* by using a radioactive tracer. In the last 20 years, particularly, advances in detector technology and computed power have made functional imaging even more applicable in diagnosing a disease and for monitoring the response of disease to treatment.

SPECT is based on the use of tracers which emit gamma rays with energy between 160 – 500 keV. Individual photons are detected using either a rotating gamma camera or special purpose multi-detector devices. All detectors used for single photon imaging require some form of gamma ray collimation and, particularly, sensitivity. The development of new radiopharmaceuticals has enable SPECT to estimate tissue functionality. One of the common radiotracers used for brain imaging is Tc-99m, also known as Tc-99m-HMPAO or Ceretec. Tc-99m is a lipid soluble macro-cyclic amine that passes through Blood Brain Barrier (BBB). Then, it converts into a hydrophilic compound in the presence of intracellular glutathione and it is trapped. The brain uptake of Tc-99m maximizes within 10 minutes of the post-injection time. The half-life of the Tc-99m is about 6 hours. This method has gained prevalence due to its low cost, producing of the image function of organ, and simple process with immediate results (Ott R, 1994).

PET uses radioactive tracers labeled with radionuclide emitting positrons during their radioactive decay. The subsequent positron annihilation within a millimeter or so of the emission point leads to the production of two 511keV gamma rays that are 180° apart. PET is performed by surrounding the object with a positron camera which records data only when two gamma rays are detected in fast time coincidence. This electronic collimation means that PET has increased sensitivity and improved spatial resolution in comparison to SPECT. The most commonly used pharmaceutical in PET is ^{18}F-flurodeoxyglucose (FDG). Since the isotopes that PET uses have short half life (e.g. ^{15}O and FDG have half lives of 2 minutes and 109 minutes, respectively), it requires an onsite cyclotron for preparation of radioisotopes which could be expensive.

PET and SPECT are important functional brain imaging in providing important tools for both diagnosis and monitoring the effects of treatment of patients with broad range of diseases. However, due to their invasiveness, radioactivity, and low resolution; a motivation has aroused to look for better techniques.

Magnetic Resonance Imaging

Magnetic Resonance Imaging (MRI) has become a popular alternative to the more traditional and well-established nuclear medicine techniques. MRI is an imaging modality that can provide image contrast based on the abundance of

hydrogen nuclei or protons with high temporal and spatial resolution. Basically, the body's protons are aligned with the direction of scanner's static magnetic field. Then, a second Radio Frequency (RF) is turned on causing protons to absorb some of its energy. When the RF is turned off, protons release their energy at a specific frequency that could be detected by the scanner. Traditionally, MR images are structural (e.g. T1); However, recent progress in developing MRI techniques has made the quantitative measurement of vascular parameters possible. This technique can produce high resolution images non-invasively or minimal invasiveness and high spatial resolution (Lauterbur PC, 1989; Wikipedia, 2009).

Two main categories of MRI techniques have been used to measure the CBF. In one category, termed Dynamic Susceptibility Contrast MRI (DSC-MRI), a paramagnetic contrast agent (e.g. Gd-DTPA) is administered intravenously and a rapid image acquisition sequence,T2*-weighted, is used to monitor the MR signal intensity during the first pass of the agent through the microvasculature (Grubb RL, Jr. *et al.*, 1974; Laniado M et al., 1984; Ostergaard L, AG Sorensen et al., 1996; Ostergaard L, RM Weisskoff et al., 1996; Rosen BR et al., 1990; Weinmann HJ et al., 1984). Using a tracer model based on the central volume theorem and the Fick principle (Ostergaard L, RM Weisskoff *et al.*, 1996), one can estimate CBF from the bolus-tracking curve. In the other category, termed Arterial Spin Labeling (ASL) MRI (Detre JA et al., 1992; Williams DS et al.,

1992), the arterial blood in the feeding artery is magnetically and non-invasively labeled and an image is acquired after a time delay (i.e. labeled image). A second image (i.e. control image) can be acquired in the same manner except that the incoming blood is not magnetically labeled and all the spins in the brain are aligned with static magnetic field, B0. The subtraction of label from control image provides an image that is proportional to the CBF, also called relative CBF (rCBF). Both techniques have been used widely for CBF measurements with the second category having the advantage of complete non-invasiveness.

Arterial Spin Labeling MRI

A new MR method called ASL is able to detect blood flow changes, non-invasively. Basically, ASL MRI magnetically labels inflowing hydrogen protons of internal carotid artery (ICA) and vertebral artery (VA) blood in the neck region. The labeled protons in blood act as endogenous tracers. They are exchanged with the water protons in brain tissue as the blood flows into the capillary. At a steady-state of this exchange, the concentration of the labeled protons in brain tissue reflects the amount of blood perfusion which is weighted by regional T1 relaxation.

There are three major categories for ASL: Continuous ASL (CASL), Pulsed ASL (PASL), and Pseudo-Continuous ASL (PCASL). In *CASL technique*, a separate coil continuously inverts the blood's protons of feeding arteries of the

brain while the head coil captures the image of whole brain. *PASL technique* selectively inverts the protons by transmitting a single radiofrequency (high tagging efficiency) and images a particular part of the brain (partial brain coverage) due to T1 relaxation of the protons. CASL method has high SNR and covers the whole brain. However, it suffers from a low tagging efficiency. The longer steady state tagging provides higher Signal to Noise Ratio (SNR). *PCASL*, as an intermediate method between CASL and PASL, employs a train of discrete pulses to mimic continuous tagging that are often unavailable on scanners due to the requirement of the second tagging coil. PCASL has the advantage of high SNR of CASL and high tagging efficiency of PASL. This is accomplished by labeling the incoming blood for a period of time (e.g. 1.6 seconds) and waiting for a period of time (1.5 seconds) before imaging the whole brain. In all three techniques the difference between two sets of images attribute to flow in the imaging plane.

PCASL MRI Theory

The analysis of MR signal in presence of magnetic gradients is described by Bloch equation, as shown below.

$$\frac{d\vec{M}}{dt} = \gamma\vec{M} \times \vec{B} + \frac{1}{T_1}\left(\overrightarrow{M_0} - \overrightarrow{M_z}\right) - \frac{1}{T_2}\left(\overrightarrow{M_x} + \overrightarrow{M_y}\right) \qquad [1]$$

If spins, constituting M, do not interact with each other or their local environment, but only with the external field (B), then these spins will experience a twisting force or a torque, given by M X B. Torque of the system is equal to time rate of change of its angular momentum, and the magnetic moment is proportional to angular moment through gyromagnetic ratio, γ. When $B=B_0$ is constant, this equation will predict that the motion of M will be a simple precession around B_0 with frequency of $w=\gamma*B_0$.

If the spins however, interact with each other and their environment, M will not precess around B_0 indefinitely but seek to return to its initial alignment parallel to B_0 with equilibrium magnitude M_0. So, the spin system needs to release energy back to environment, called relaxation. Two time constants, called T1 and T2. T1 for the re-growth of longitudinal magnetization component (Mz) and T2 decay of the transverse component (Mx and My).

As explained previously, ASL MRI acquires CBF map by calculating the difference between control and label images. This technique only focuses on T1 term (z magnetization), second term of equation 1. So, the net magnetization of spins depends on T1 term, in-flow magnetization of blood, and out-flow magnetization of blood, shown in equation 2.

$$\frac{dM_z(t)}{dt} = \frac{1}{T_{1.b}}\left(M_b^0 - M_b(t)\right) + fM_a(t) - fM_v(t) \qquad [2]$$

Where M, M_a, and M_v are the *z*-magnetization of the tissue water, arterial, and venous blood, respectively, M_0 is the equilibrium value of M, T_1 is the spin lattice relaxation time of brain water in the absence of perfusion and λ is the brain-blood partition coefficient of water.

Control Image

In order to simplify, I assumed that under fully relaxed conditions, the magnetization of brain water and arterial blood (no inversion) are equal, $M_a(t) = M_b^o/\lambda$ and Magnetization of spins in the venous outflow is equal to brain tissue, $M_v(t) = M_b(t)/\lambda$, shown in equation 3.

$$\frac{dM_z(t)}{dt} = \frac{1}{T_{1.b}}\left(M_b^0 - M_b(t)\right) + {}^{f}/_{\lambda}\, M_b^0 - {}^{f}/_{\lambda}\, M_b(t) \qquad [3]$$

After solving the equation for $M_b(t=0)$ (i.e. control image) and replacing $\left(\frac{1}{T_1} + \frac{f}{\lambda}\right) = \frac{1}{T_{1app}}$, the control image becomes

$$M_b(0) = M_b^0 \qquad [4]$$

Labeled Image

The arterial spins are continuously inverted by 180°, $M_a(t) = -M_a^o$ and once the brain tissue is saturated with inverted arterial blood, the magnetization of

brain tissue becomes the magnetization of blood, $M_a^o = M_b^o/\lambda$. Thus, the magnetization of brain tissue becomes $M_a(t) = -M_b^o/\lambda$. So the equation 3 can be rewritten as

$$\frac{dM_z(t)}{dt} = \frac{1}{T_1}\left(M_b^0 - M_b(t)\right) - f/\lambda\, M_b^0 - f/\lambda\, M_b(t) \qquad [5]$$

After solving the equation for $M_b(t=\infty)$ or $M^{ss}{}_b$, the labeling image becomes

$$M_b^{ss} = M_b^0 \frac{\left(1 - \frac{fT_1}{\lambda}\right)}{\left(1 + \frac{fT_1}{\lambda}\right)} \qquad [6]$$

Difference Image

The difference between control [4] and label [6] becomes:

$$M_b^0 - M_b^{ss} = 2M_b^0\, f/\lambda\, T_{1app} \qquad [7]$$

When considering T1 decay and Alpha, α, the difference becomes:

$$\Delta M = M_b^0 - M_b^{ss} = \left(2\alpha M_b^0\, f/\lambda\, T_{1app}\right) e^{-\delta/T_{1a}} \qquad [8]$$

Where the arterial transit time, δ, from tagging plane to imaging plane is considered to be 0 and α is inversion efficiency which equals 1 for a perfect inversion.

Note that signal, ΔM , in equation 8 is exponentially dependent on the arterial transit time, δ, if it is not equal to zero. This variation in arterial transit time for different brain regions affects the observed signal and the perfusion measurement. In human studies, the measurement of the transit time is critical and an accurate measurement of this physiological parameter is challenging. In order to overcome this problem, Alsop et al. proposed a waiting time (w) after tagging blood and before imaging.

$$M_b^0 - M_b^{ss} = \left(2\alpha M_b^0 \, f/\lambda \, T_{1app}\right) e^{-\delta/T_{1a}} \cdot e^{\left(\frac{\min((\delta - w),0)}{T_{1app}}\right)} \quad [9]$$

If w > δ, the expression becomes:

$$M_b^0 - M_b^{ss} = \left(2\alpha M_b^0 \, f/\lambda \, T_{1app}\right) e^{-\delta/T_{1a}} \cdot e^{\left(\frac{\delta - w}{T_{1app}}\right)} \quad [10]$$

Figure 3 shows three stages where the image difference was derived. After labeling period, the difference image was calculated based on equation 7. After transit time δ, the image difference is calculated based on equation 8.

Lastly, after a waiting period, w, the difference image is calculated based on equation 10.

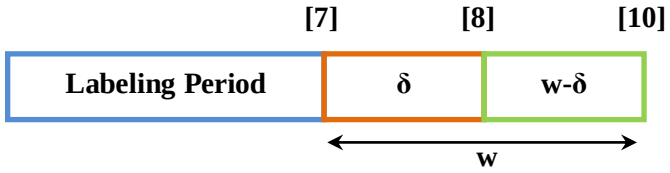

Figure 3: The diagram above shows various stages of difference image calculated. The number above each box corresponds to equation number which was derived previously.

In figure 4, the simulation of equation 10 is shown with solid line. The highest signal is at time zero but the signal degrades considerably at the transit time increases. After introducing delay time, w, the signal becomes very insensitive to transit time. According to Lu et al. 2004, the T1 of blood in 3T magnet field is 1.624 seconds; thus, the labeled blood can be measured with a waiting period of 1.5 seconds, as shown below, before the protons are fully relaxed.

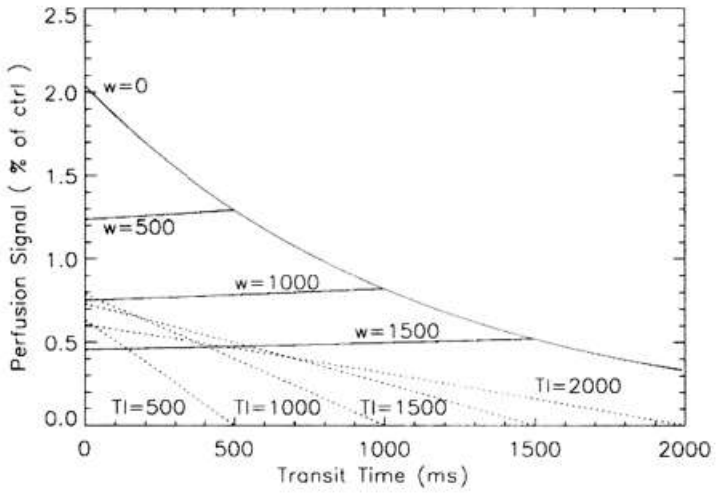

Figure 4: Theoretical image signal intensity for a flow of 60 ml per 100 grams per minute as a function of tissue transit time for continuous and pulsed inversion experiment in gray matter. The solid line denotes the CASL and the dotted line shows PASL. Our PCASL method follows the CASL trend line. This figure is replicated from Alsop et al article.

In our PCASL model, I will utilize a delay time, as shown above, to avoid transit time estimation and reduce the effect of arteries with high signal intensity.

Phase Contrast MRI Theory

Phase Contrast MRI (PC MRI) was used in combination with pCASL MRI to estimate absolute blood flow of brain. PC MRI utilizes the phase of an image to encode the velocity of moving spins. As shown in figure 5, PC MRI is a typical gradient-echo sequence except that a bipolar gradient is inserted before the data acquisition to encode the velocity. The mechanism of velocity encoding can be seen with the following descriptions. The application of magnetic field gradient causes magnetization phase change. Assuming a base phase of for the magnetization, the addition of one lobe of gradient would result in a phase of

$$\varphi = \gamma \times G \times z_1 \times t + \phi_0 \quad [11]$$

where γ is the gyromagnetic ratio, G is the magnitude of the gradient, z1 is the coordinate of the spin along z direction at this time, t is the duration of the lobe, ϕ_0 is the base phase due to field inhomogeneity, eddy current and other factors. The second gradient is applied with opposite direction; therefore, the phase has a negative sign. The phase becomes

$$\phi_a = \gamma \cdot G \cdot z_1 \cdot t - \gamma \cdot G \cdot z_2 \cdot t + \phi_0 \quad [12]$$

$$\phi_a = \gamma \cdot G \cdot (z_1 - z_2) \cdot t + \phi_0 = -\gamma \cdot G \cdot v \cdot t^2 + \phi_0 \quad [13]$$

where v is the flow velocity. During the next TR period, the order of the gradients is reversed. Thus the phase for the second TR will be

$$\Delta\phi_b = 2\gamma \cdot G \cdot v \cdot t^2 \quad [14]$$

A subtraction ϕ_a between and ϕ_b will remove the ϕ_0 effect, yielding a phase value that is solely dependent on the flow velocity $\Delta\phi_b = 2\gamma \cdot G \cdot v \cdot t^2$ from which the velocity map within the vessel can be calculated. Integrating the velocity inside the vessel of interest will give total flux (in ml blood/min) for this vessel. Note that, although the measurement of velocity is sensitive to the orientation of the slice (ideally should be perpendicular), the total flux is relatively insensitive to the orientation because the area of the cross-section (*A*) will cancel the angle effect:

$$Flux_{measured} = v_{measured} \cdot A_{measured} = v_{true} \cdot \sin(\theta) \cdot$$
$$A_{true}/\sin\theta = v_{true} \cdot A_{true} = Flux_{true} \quad [15]$$

The PC MRI is a relatively well-established technique, and is a standard sequence on our Philips MRI system.

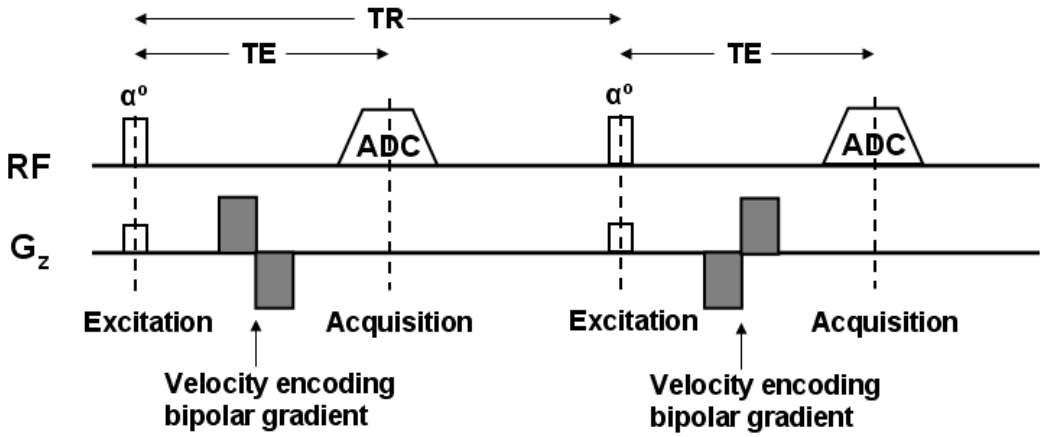

Figure 5: Phase-contrast MRI pulse sequence. Two successive TR periods are shown. The only difference between the two periods is the sign of the velocity encoding gradient. This paired scheme is used so that a subtraction would remove any spurious phases due to field inhomogeneity and eddy current.

The current work is composed of three major parts. In the first investigation, I estimated absolute cerebral perfusion by combining pCASL and PC MRI and detected the aCBF change in brain perfusion under hypercapnia. The results of this experiment are published in Magnetic Resonance in Medicine (MRM) journal. In the second study, I showed that pCASL can detect regional CBF difference by "modeling" control and patient group. I also showed that by normalizing CBF map I am able to improve the detection rate significantly. The results of this experiment are published in Magnetic Resonance Imaging (MRI) journal. In the final study, I measured CBF in white matter fibers by combining DTI and pCASL MRI. The result of this study suggests that fibers' CBF and myelination (i.e. FA) are inversely correlated. Furthermore, the regions that are functionally correlated have higher degree of fiber myelination that structurally connect them. This indicates that the action potential along these fibers may be conducting more efficiently. The results of this study will be submitted to Cerebral Cortex journal.

SPECIFIC AIM 1: ESTIMATION OF LABELING EFFICIENCY IN PSEUDO-CONTINUOUS ARTERIAL SPIN LABELING

INTRODUCTION

Arterial Spin Labeling (ASL) MRI is a non-invasive technique that can measure Cerebral Blood Flow (CBF) (Detre JA *et al.*, 1992). ASL MRI have two major categories, Continuous ASL (CASL) (O'Gorman RL et al., 2006; Trampel R et al., 2004; Wang J et al., 2005; Williams DS *et al.*, 1992; Wong EC et al., 1998) and Pulsed ASL (PASL) (Alsop DC and JA Detre, 1996; Golay X et al., 1999; Hendrikse J et al., 2003; Kim SG, 1995; Kwong KK et al., 1995; Petersen ET et al., 2006; Yang Y et al., 1998). CASL technique utilizes continuous adiabatic inversion whereas PASL employs a single inversion pulse. In CASL, due to long steady state tagging, this technique often has high power disposition and sometimes requires a second RF coil for spin labeling (Detre JA and DC Alsop, 1999; Wolff SD and RS Balaban, 1989). Therefore, it has not be widely used compared to PASL (Gunther M et al., 2005; Wong EC *et al.*, 1998), which is simpler in implementation.

The recently developed Pseudo Continuous ASL (pCASL) MRI is an intermediate technique between CASL and PASL (Dai W et al., 2008; Garcia DM dBC, Alsop DC, 2005; Wong EC, 2007; Wu WC et al., 2007). This technique utilizes a series of discrete RF pulses to mimic the CASL method for spin labeling. One of the most critical parameters of the pCASL method that could affect perfusion quantification and the quality of perfusion images is the labeling efficiency, α, defined as (arterial blood in the control scan – arterial blood in the

label scan)/2. Unlike CASL, the labeling process of pCASL is not strictly an adiabatic inversion. Thus the labeling efficiency may be dependent on B0 inhomogeneity, B1 inhomogeneity and flow velocity. Several studies have used numerical simulations to investigate the efficiency under different labeling schemes and conditions (Dai W *et al.*, 2008; Wong EC, 2007; Wu WC *et al.*, 2007). However, due to heterogeneities across subjects, arterial locations, and physiologic states, it is desirable to experimentally determine the labeling efficiency for each pCASL scan.

Here, I experimentally studied the effect of labeling efficiency in pCASL and proposed an experimental method to estimate the efficiency in vivo. Three sets of studies were performed. First, I empirically determined the optimal anatomic location to achieve the best labeling efficiency. The CBF map with the highest signal intensity was chosen as the best possible location. Second, I estimated the labeling efficiency at the optimal position by using phase-contrast (PC) velocity MRI as a normalization factor, thereby providing a method to determine α for each subject. Third, I demonstrated that labeling efficiency may change depending on physiological state. Carbon Dioxide (CO2) is a potent vasodilator and results in an increase in arterial flow velocity. I compared α during hypercapnia (inhalation of 5% CO2) to that during normocapnia (room-air breathing). Based on these data, I propose that the labeling efficiency should be estimated by using PC velocity MRI on a subject-specific basis.

MATERIALS AND METHODS

General

Experiments were performed on a 3T MR system (Philips Medical Systems, Best, the Netherlands) using body coil transmission and head coil reception. The protocol was approved by the Institutional Review Board of University of Texas Southwestern Medical Center at Dallas. A total of 25 subjects (14 male, 11 females, 21-45 years of age) were consented before participating in the study. A balanced pCASL sequence was used following previous studies by Wu et al. and Wong (Wong EC, 2007; Wu WC *et al.*, 2007). Imaging parameters for all pCASL experiments were identical: single-shot gradient-echo EPI, field-of-view (FOV)=240x240, matrix=80x80, voxel size=3x3 mm, 27 slices acquired in ascending order, slice thickness=5 mm, no gap between slices, labeling duration=1650 ms, post spin labeling delay=1525 ms, TR=4020 ms, TE= 14ms, SENSE factor 2.5, time interval between consecutive slice acquisitions=35.5 ms, number of controls/labels= 30 pairs, RF duration=0.5 ms, pause between RF pulses = 0.5 ms, labeling pulse flip angle=18°, bandwidth=2.7 kHz, echo train length=35, and scan duration 4.5 min. In addition, a high resolution T1 weighted image was acquired with the following parameters: MPRAGE sequence, TR/TE=8.3ms/3.8ms, flip angle=12°, 160 sagittal slices, voxel size=1x1x1 mm^3, FOV=256x256x160 mm^3, and duration 4 min.

Study 1

The purpose of this study was to experimentally determine the optimal location of labeling plane to achieve the highest sensitivity. Seven subjects participated in this study. With the imaging slices positioned at the same location, the labeling plane was varied to be 49, 63, 74, 84, 94, 119, 149 mm distal to the anterior-commissure (AC) posterior-commissure (PC) line since the blood is labeled in the neck region before it enters the brain (bottom panel, Figure 6).

PCASL data were motion corrected using SPM5 (Wellcome Department of Imaging Neuroscience, London, UK). An in-house MATLAB (Mathworks, Natick, MA) program was used to calculate the difference between averaged control and label images. Then, the difference image was corrected for imaging slice delay time to yield CBF-weight image, which was normalized to the Brain template from Montreal Neurological Institute (MNI) using SPM5. The normalized CBF-weighted image was spatially averaged and compared across different labeling positions.

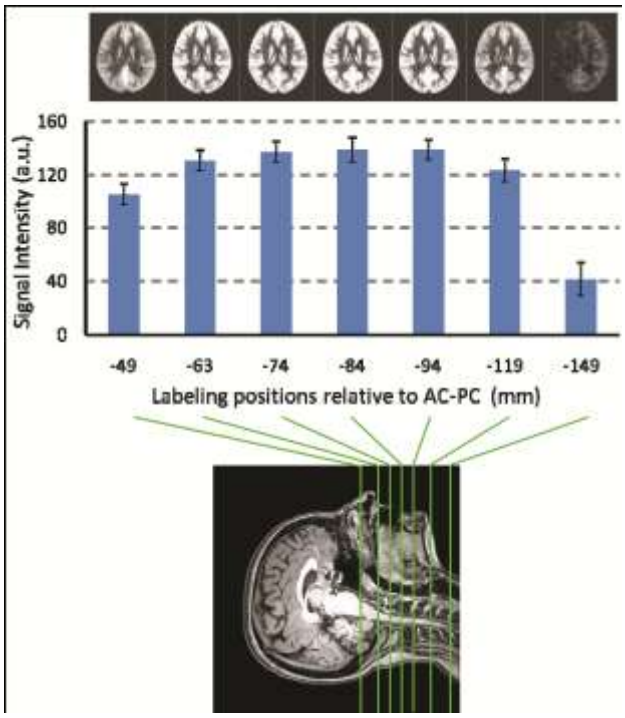

Figure 6: Intensity of CBF-weighted signal as a function of labeling position. PCASL MRI was performed with the labeling plane positioned at 7 different locations (bottom panel). The locations are in reference to the AC-PC line. The top panel shows average CBF-weighted images at each location. Image intensity change as a function of labeling position can be visually observed. Error bars indicate standard errors of mean.

Study 2

The goal of this study was to estimate labeling efficiency of pCASL method utilizing PC velocity MRI as a normalization factor. PC velocity MRI uses bipolar gradients to modulate the phase of flowing spins and, under the assumption of minimal velocity variation across a voxel and negligible outflow effect, can provide an estimation of flow velocity (Haacke EM BR, Thompson

MR, Venkatesan R, 1999). Ten subjects were scanned by placing the labeling slab at the optimal position determined in Study 1. In addition to the pCASL scan, a time-of-flight (TOF) angiogram and a PC velocity MRI were performed. The TOF angiogram was performed to visualize the internal carotid arteries (ICA) and vertebral arteries (VA), and to correctly position the PC velocity MRI slice (Figure 7b). The imaging parameters were: TR/TE/flip angle=23ms/3.45ms/18°, FOV=160x70x160mm^3, voxel size 1.0x1.0x1.5mm^3, number of slices =47, one saturation slab of 60mm positioned above the imaging slab to suppress the venous vessels, duration 1 min 26 sec. The slice of the PC velocity MRI was oriented perpendicular to the ICA and VA (Figure 7b) and the parameters were: single slice, voxel size=0.45x0.45 mm^2, FOV=230x230 mm^2, TR/TE=20/7 msec, flip angle=15°, slice thickness=5 mm, maximum velocity encoding=80 cm/s, and scan duration=30 sec.

PC velocity MRI provides a quantitative measurement of blood flow velocity, v, in ICA and VA. The blood velocity can be converted to flow rate by integrating over the cross-section of the vessels. The flow, F, is calculated by:

$$F = \int v dA \qquad [16]$$

The unit of F is ml blood/second, i.e. blood influx per unit time. The PC velocity MRI was conducted at the level of cervical spine C2 above the bifurcation of carotid arteries. Anatomy literature established that there are no extracranial branches at this level (Gray H, 1988). VA, on the other hand, may

have small branches perfusing spinal cord, which may cause an over-estimation of brain blood flow. Such branches, however, are not visible in the TOF angiogram, suggesting that the effect, if any, is minimal. Thus the value of F indicates the sum of blood flow of the whole brain. I then divided F by the intracranial mass (calculated from T1W image and by assuming brain density of ρ =1.06 g/ml (Herscovitch P and ME Raichle, 1985)) and obtained the normalization factor, $f_{PC,AVG}$, which is the whole brain averaged blood flow in units of ml blood/sec/g brain or ml blood/min/100g brain. On the other hand, pCASL can also give an estimation of blood flow using an equation from Alsop and Detre (Alsop DC and JA Detre, 1996):

$$f_{pCASL}(x,y,z) = \frac{\lambda \cdot e^{\left(\frac{\delta}{T_{1a}}\right)}}{-2\alpha \cdot M_b^0 \cdot T_1 \cdot \left[e^{\left(\frac{\min(\delta - w_z, 0)}{T_1}\right)} - e^{\left(\frac{-w_z}{T_1}\right)\left(1-\frac{T_{1RF}}{T_1}\right)} \right]} \times \Delta M(x,y,z) \quad [17]$$

where $f_{pCASL}(x,y,z)$ is the blood flow value at voxel (x,y,z) obtained from pCASL in ml blood/min/100g brain; α is the labeling efficiency; λ is the blood-brain partition coefficient (0.98 ml/gram (Herscovitch P and ME Raichle, 1985)); δ is the arterial transit time of blood from the tagging plane to the imaging slice (assumed to be 2 seconds (Alsop DC and JA Detre, 1996)); w is the delay

between the end of labeling and the start of acquisition (1.525 seconds); T_1 is the brain tissue T_1 (1.165 seconds (Lu H et al., 2005)); T_{1a} is the T_1 of arterial blood (1.624 seconds (Lu H et al., 2004)); T_{1RF} is the is the T_1 in the presence of off-resonance irradiation (0.75 seconds (Oguz KK et al., 2003)); M_b^0 is the value of equilibrium magnetization of brain tissue, which was obtained from manual ROI drawing of thalamus in the control image by $M_b^0 = M_{thal}/(1-e^{-TR/T_{1,thal}})$ and assuming $T_{1,thal}$ = 0.986 seconds (Lu H *et al.*, 2005). I chose to draw the ROIs in the thalamus because it is gray matter and the structure thickness is sufficient for manual drawing (cortical gray matter can be very thin). Note also that both ΔM and M_b^0 contain T2* effect and they tend to cancel out after the division.

Summing values for Eq 13, one then obtains:

$$f_{pCASL,AVG} = \frac{1}{\alpha}\sum_{x,y,z}\left\{\frac{\lambda \cdot e^{\left(\frac{\delta}{T_{1a}}\right)}}{-2 \cdot M_b^0 \cdot T_1 \cdot \left[e^{\left(\frac{\min(\delta - w_z, 0)}{T_1}\right)} - e^{\left(\frac{-w_z}{T_1}\right)\left(1-\frac{T_{1RF}}{T_1}\right)}\right]} \times \Delta M(x, y, z)\right\} / N_{WB} \quad [18]$$

where N_{WB} is the total number of pCASL voxels inside the intracranial space. I can then equate the blood flow measured from PC velocity MRI and pCASL MRI, i.e. $f_{PC,AVG}=f_{pCASL,AVG}$, and the only unknown in the equation is α which is estimated. Conceptually, this normalization method can be viewed as follows: Adding up all the pCASL signals within the brain gives the total amount of MRI

signal in arbitrary unit (a.u.). On the other hand, the phase contrast scan gives the total amount of CBF in ml/min. These two are essentially equivalent. Thus, one can obtain the "conversion rate" that indicates each unit of MR signal is worth how much CBF. Once the labeling efficiency is known, the absolute CBF map can be calculated with Eq. [18].

For data processing of PC velocity MRI, a preliminary ROI was drawn on each of the four arteries (left and right ICA, left and right VA) based on the magnitude image (Figure 7d). The operator was instructed to trace the boundary of the targeted vessel without including adjacent vessels. A signal intensity threshold (2 x noise level) was then applied to the magnitude image to remove any background voxels and to obtain the final vessel mask. The final mask was applied to the velocity map (i.e. the phase image of PC velocity MRI, Figure 7e) and the total flow, F, inside the mask was calculated according to Eq. [16].

Regional CBF values for gray and white matters were quantified by manually placing ROIs in corresponding regions for each subject.

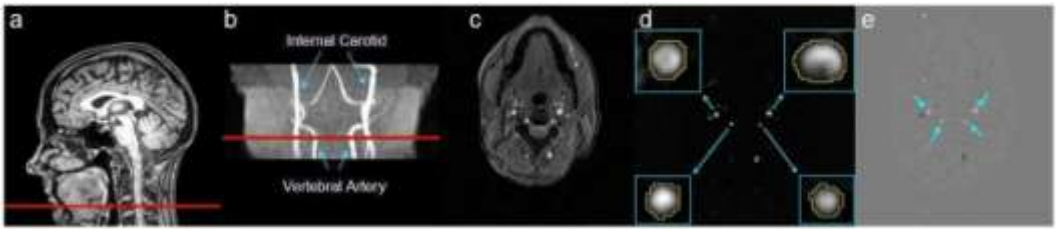

Figure 7: Phase-contrast (PC) velocity MRI of Internal Carotid Arteries (ICA) and Vertebral Arteries (VA). (a) Location of the slice of PC

velocity MRI on a mid-sagittal image. (b) Location of the PC velocity MRI on the angiogram. (c) Raw image of PC velocity MRI. (d) Magnitude image of PC velocity MRI. The insets show the left and right ICAs and VAs as well as the manually drawn ROIs. (e) Velocity map from the PC velocity MRI. Positive value indicates inflow blood, often corresponding to arteries, whereas negative value indicates outflow blood, typically from veins.

Study 3

In the third study, I investigated whether or not the labeling efficiency in pCASL is dependent on the subject's physiologic state. Hypercapnia was induced using 5% CO2 breathing and it is known to increase blood flow in the entire brain. Eight subjects wore nose clips and breathed via a mouth piece while they were scanned in a supine position. End Tidal CO2 (etCO2), breathing rate (BR), heart rate (HR) and arterial oxygenation saturation (spO2) (Capnogard, Model 1265, Novametrix Medical Systems, CT, and MEDRAD, Pittsburgh, PA) were also monitored and recorded continuously on a laptop. The subjects first inhaled normal room-air for 7 minutes while TOF angiogram, pCASL, arterial PC velocity MRI, and sagittal sinus PC velocity MRI scans were performed. Then, the one way valve, to avoid re-breathing, was switched to hypercapnia gas mixture (5% CO2, 74% N2 and 21% O2) contained within a Douglas bag. Based on our experience, I allotted two minutes of waiting time to allow the physiology to stabilize at the hypercapnic state. Then, I finalized our study by performing a pCASL, arterial PC velocity MRI, and saggital sinus PC velocity MRI scans.

Hypercapnia-induced changes in CBF-weighted signals, i.e. $\Delta M=S_{control}-S_{label}$, were calculated using pCASL MRI. These results were compared to those obtained from arterial PC velocity MRI and sagittal sinus PC velocity MRI. The labeling efficiencies of pCASL under normocapnic and hypercapnic states were also estimated using methods described in Study 2.

RESULTS

Study 1

Figure 6 shows the CBF-weighted signal intensity as a function of labeling position. The average CBF maps for each position are shown at the top of Figure 6. Quantitative analysis revealed that the averaged signal intensity is highest when the label plane is positioned at 84mm below the AC-PC line. For individual subjects, the peak location was 78.1±3.8mm (mean±SD). CBF-weighted signal at 149mm was significantly lower than all other labeling positions ($p<0.001$ for pair-wise t tests) due to B1 power decay of the body transmission coil at distant location. When the labeling plane is very close to the brain (49mm below AC-PC), the CBF-weighted signal is also lower than the peak signal ($p<0.005$), possibly due to the variant vessel orientation in this region.

Study 2

Figure 7 illustrates the slice location of PC velocity MRI and representative PC velocity images. Using the PC velocity MRI and T1W MPRAGE data, whole brain blood flow (F), intracranial volume and unit mass blood flow ($f_{PC,AVG}$) were calculated to be 730.1±97.1 ml/min (n=10, mean±SD), 1508.5±188.2ml and 46.0±6.3 ml/min/100g, respectively. Considering that the data analysis of PC velocity MRI involves manual ROI drawing and this step may introduce rater-dependence in the quantification of F, I performed an inter-rater reliability test by having two researchers (SA and FX) each processing 50 vessels with a range of sizes. I observed a high inter-rater reliability (r^2=0.99, $p<0.001$). Using the PC velocity MRI results and Eq. [13], the labeling efficiency of pCASL was estimated to be 0.86±0.06 (n=10, mean±SD, range 0.79-0.98), in good agreement with simulation results reported by Wu et al. (Wu WC *et al.*, 2007). After the labeling efficiency is determined, absolute CBF maps were computed using Eq. [12]. Whole brain averaged gray and white matter CBF were 55.0±8.4 ml/min/100g and 21.0±5.2 ml/min/100g, respectively, with a gray/white ratio of 2.7±0.5. These perfusion results are consistent with other techniques such as DCS MRI and PET (Leenders KL et al., 1990; Rempp KA et al., 1994; Vonken EJ et al., 1999; Ye FQ et al., 2000). Table 1 shows regional CBF values for gray and white matters. Parietal white matter had smaller ($p<0.03$) CBF compared to frontal and occipital white matters. No other regional differences were found for

cortical gray matter or white matter. CBF values of deep gray matter were between white matter and cortical gray matter.

Table 1: Regional CBF values (ml/min/100g) as measured from pCASL MRI (mean±SD, n=10).

Frontal GM	Parietal GM	Occipital GM	Frontal WM	Parietal WM	Occipital WM	Caudate	Putamen
54.7±9.7	54.9±9.0	55.4±10.0	23.7±6.8	15.7±6.4	23.6±7.6	52.4±18.5	45.4±10.1

Study 3

Inhalation of 5% CO2 increased the Et-CO2 from 40.2±3.8 mmHg to 49.1±2.4 mmHg (n=8, mean±SD), but did not change arterial oxygenation or heart rate significantly, as shown in figure 8. On average, PC velocity MRI in ICAs and VAs showed a whole brain CBF increase of 59.6±24.3% comparing hypercapnia to normocapnia. For confirmation, I also performed PC velocity MRI in sagittal sinus, which showed similar increases (62.2±29.7%) in global CBF. For pCASL, if I do not consider the possible changes in labeling efficiency between normocapnia and hypercapnia, and just use the CBF-weighted signal, $\Delta M=S_{control}-S_{label}$ (as used in most ASL fMRI or physiologic challenge studies), the increases in ΔM were 40.1±20.3%. This is considerably lower ($p=0.01$) than that using PC velocity MRI. I attribute this discrepancy to a reduction in labeling efficiency from normocapnia to hypercapnia due to higher blood velocity. The labeling efficiency were estimated to be 0.95±0.10 (n=8, mean±SD) and

0.84±0.09, respectively (p=0.025, paired t test), using the method described in Study 2. Figure 9 shows absolute CBF maps of normocapnia, hypercapnia and difference between hypercapnia and normocapnia, after accounting for the labeling efficiency in each physiologic condition.

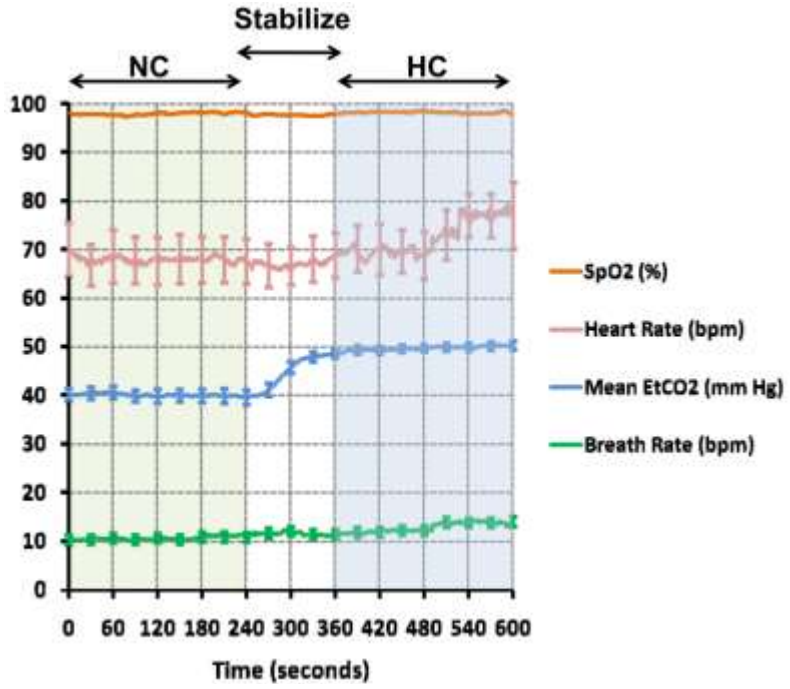

Figure 8: Physiologic parameters during normocapnia and hypercapnia. The parameters are shown as a function of time. Error bars indicate standard errors of mean. The end-tidal CO2 increased ($p<0.0001$) from normocapnia to hypercapnia, but the other parameters did not show a significant change ($p>0.1$).

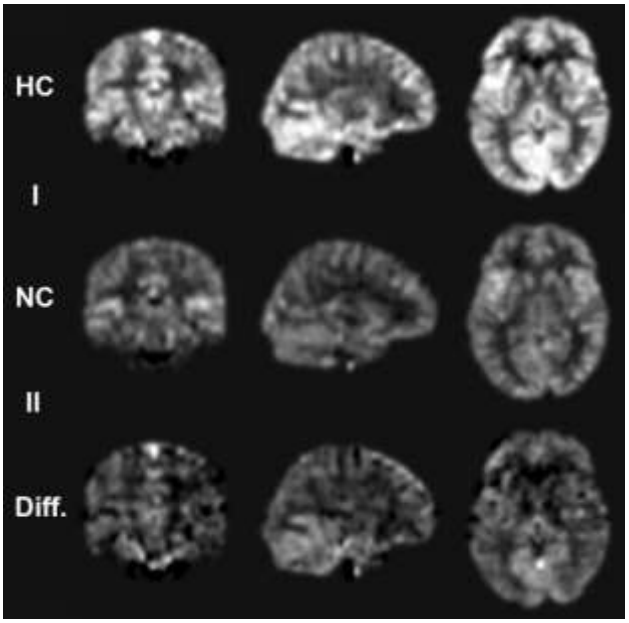

Figure 9: Representative CBF maps during normocapnia and hypercapnia as well their differences. The data have been spatially normalized to the MNI brain template. The quantification of CBF used Eq. [12] and the experimentally estimated labeling efficiency. CBF increases can be seen in the entire brain.

I note that the estimated labeling efficiency during normocapnia appears to be higher than that in Study 2. Aside from a possible contribution of age differences between the two groups (35±10 yrs and 29±7 yrs for studies 2 and 3, respectively), another potential reason is that the subject tends to slightly hyperventilate when breathing through the mouth piece. As a result, the flow may be lower than the regular breathing conditions, and the labeling efficiency becomes higher. This is confirmed from the whole brain flow values (46.0±6.3 ml/min/100g and 42.8±8.2 ml/min/100g for studies 2 and 3, respectively).

Finally, I studied the correlation between the labeling efficiency and arterial flow velocity across subjects and physiologic states (total 26 measurements) (Figure 10). A significant correlation was observed (r=-0.46, p=0.02), in general agreement with predictions from numerical simulations (dashed curve in Figure 10) (Wu WC *et al.*, 2007).

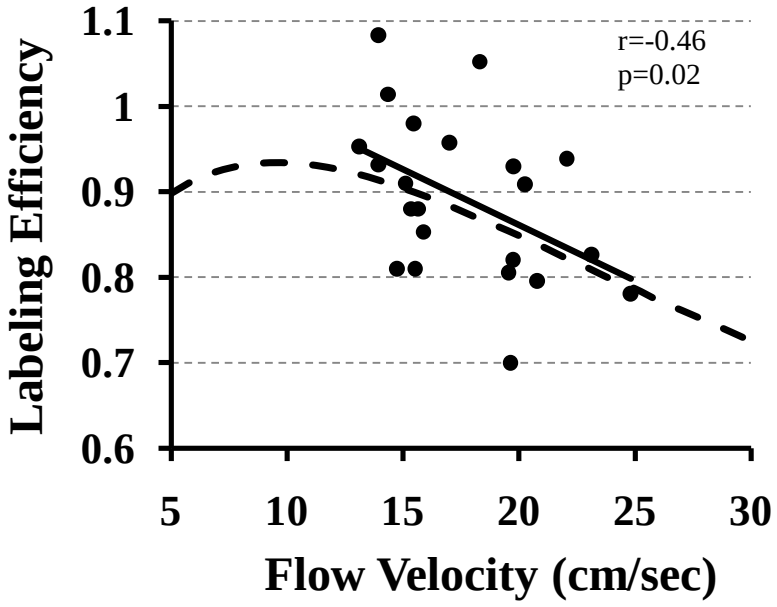

Figure 10: Experimental and simulation data of pCASL labeling efficiency as a function of flow velocity. The experimental data (filled dots) were from all subjects in Studies 2 and 3 (26 measurements). The solid line is the linear fitting of the experimental data. The simulation (dashed curve) used sequence parameters identical to those used in the experiments: RF duration=0.5 ms, pause between RF pulses=0.5 ms, labeling pulse flip angle=18°. The spins were assumed to be on-resonance and flowing at a constant velocity. The experimental data showed a significant correlation between labeling efficiency and flow velocity (r=-0.46, p=0.02).

DISCUSSION

In this study, I investigated several questions related to labeling efficiency in pCASL MRI. I performed pCASL labeling at different anatomic locations and determined that labeling at 84mm below the AC-PC line yielded the highest signal intensity, although the curve was relatively flat within the range of 74-94mm. Next, I proposed an experimental method to estimate the labeling efficiency for each subject based on whole brain CBF obtained from PC velocity MRI. Finally, I demonstrated that the labeling efficiency is not only subject-dependent but can also vary with physiologic conditions, because arterial flow velocity may be altered with vascular challenge or neural activation. Based on these findings, I recommend that the labeling efficiency in pCASL MRI should be estimated on a subject-specific and physiologic-condition-specific basis.

ASL MRI is a powerful technique and, in recent year, many interests have developed to apply this technique to the studies of neurological and psychiatric disorders, a niche field conventionally occupied by SPECT and PET imaging (van Osch MJ et al., 2009; Williams DS *et al.*, 1992). Researchers especially clinical-oriented ones often seek a technique that is quantitative, easy to implement (e.g. no coil change, no contrast agent), short in duration (e.g. 5 min), and covers the whole brain, similar to T1, T2, FLAIR or DTI techniques. In this regard, a few traits of pCASL MRI such as high sensitivity, large brain coverage, and no need for special hardware (Fernandez-Seara MA et al., 2008; Wong EC, 2007; Wu WC

et al., 2007) are particularly attractive. Compared to conventional ASL methods, pCASL MRI introduces minimal number of new caveats. One new issue that may be specific to pCASL is the uncertainty in labeling efficiency, because the labeling mechanism of pCASL is no longer based on adiabatic inversion and any variations in B0, B1, or flow velocity may have a significant impact on the efficiency. This is particularly relevant when one aims to conduct quantitative comparison of CBF between patient populations or in the same population before and after various interventions, including medication. Therefore, an experimental method to quantify the labeling efficiency in pCASL may provide an important piece of puzzle in preparing ASL MRI for large scale clinical research or routine clinical MRI scan.

Several previous studies have pointed out the importance of labeling efficiency in pCASL. Wong conducted numerical simulations and showed that the labeling efficiency is lower when the resonance frequency is shifted from the center frequency due to B0 inhomogeneity (Wong EC, 2007). Wu et al. and Dai et al. have reported pCASL labeling efficiency by using CASL as a reference (Dai W *et al.*, 2008; Wu WC *et al.*, 2007) . They conducted pCASL and conventional CASL MRI in the same participants and the differences in signal amplitude are attributed to differences in labeling efficiencies. By further assuming the CASL labeling efficiency from previous simulations by Maccotta et al. (Maccotta L et al., 1997), the labeling efficiency in pCASL was estimated. One potential

confounding factor is that the simulation results may not be applicable for the specific hardware and sequence parameters used in a given study. A second drawback is that it is not practical to conduct pCASL and CASL comparison in every study, thus the labeling efficiency cannot be estimated on a subject-by-subject basis. On the other hand, the approach used in the present study is independent of previous simulations and can be easily applied without changing RF coil.

The method to estimate labeling efficiency proposed in this study is based on normalization of pCASL signal with PC velocity MRI. The scan time for PC velocity MRI is only 0.5 min. However, in order to position the PC velocity MRI slice, a TOF angiogram was acquired in our study, adding another 1.5 min to the session duration. Therefore additional 2-3 minutes of scan time is needed for our proposed technique. This is an approximately 40-50% increase compared to a conventional ASL scan of about 5 minutes. This may be particularly challenging for clinical scans where the total duration of the session is less than 20 minutes. In addition, extra data processing is needed compared to conventional ASL. The processing of the PC velocity data involves manual drawing of four ROIs covering left/right internal carotid and vertebral arteries, respectively. Our processing scripts are optimized and this typically takes less than 3 minutes. At present, I am doing the processing offline because I am not using velocity information for any real time adjustment of the protocol. However, in the future if

I were to determine the labeling position for each subject in real time, the online processing would indeed be helpful. I would need to work with our vendor to incorporate the processing scripts in the user interface. However, in terms of the algorithm and procedure, they are quite straightforward and fast.

In the estimation of labeling efficiency from Eq. 18, the values of several variables were assumed from reports in literature. The actual values in a voxel may be slightly different from the assumed values. This will introduce error in the estimation. In particular, if there are regional differences in arterial transit time, tissue T1 or blood-brain partition coefficient, CBF in some brain regions will be over-estimated while other regions will be under-estimated. As a consequence, even though the whole brain averaged CBF is still correct, the regional values may contain errors. This issue is not specific to the efficiency estimation technique proposed in this study, but is related to ASL CBF measurement in general. If an accurate relative CBF map can be obtained with ASL, our method of quantification will also be accurate. A well-known approach to reduce arterial transit time sensitivity is to use longer delay times (Alsop DC and JA Detre, 1996). However, overall SNR will be low at long delay times.

The PC velocity MRI protocol used in this study is very short in duration (0.5 min) and is not triggered by cardiac cycle. As a result, cardiac pulsation effect causes some ghostings in the phase-encoding direction (anterior-posterior direction). To assess the potential errors of cardiac pulsation, I compared the flux

values obtained from non-gated PC and a 15-phase gated PC in additional subjects. The difference between the two techniques was found to be <3%, similar to the results from literature (Spilt A et al., 2002). Considering a 10 fold difference in scan duration, I have used the non-triggered version in this study. Another potential approach to estimate the labeling efficiency is to directly image the vessels immediately above the labeling location and to measure the magnitude and sign of the blood magnetization. For example, a signal of $-M_0$ would indicate a 100% labeling efficiency. While this approach is conceptually straightforward, there have not been reports for either CASL or pCASL estimations. Possible reasons include technical challenges in high-resolution imaging of blood vessels and the outflow effect of moving spins.

When using a fixed labeling location (84mm below AC-PC line), a range of labeling efficiencies were observed across subjects. This is partly explained by variations in arterial velocity (Figure 10) due to normal variance in vessel anatomy. If one measures vessel velocity at a few locations and determines the best labeling location for each subject (e.g. find locations where velocity is approximately 10cm/s), a more homogeneous labeling efficiency may be achieved. However, to achieve this, more PC velocity scans are needed and the operator also needs to conduct analysis on the fly. In addition, within a subject, the arterial flow velocity may change from one day to another and even within the same day, due to drug treatment, ventilation level or even consumption of caffeine

products. Therefore, it is recommended that the labeling efficiency in pCASL MRI be estimated for each subject in the same scan session. Furthermore, other factors such as B0 and B1 inhomogeneity may cause the labeling efficiency to be different across subjects. This is especially relevant in view of our finding that the optimal labeling location appears to be in the neck regions where different subjects may have different amount of dental works. The dental works will not only cause a variation in labeling efficiency, but also result in a decrease in SNR of the pCASL signals due to magnetic susceptibility artifacts. These factors need to be considered in certain clinical studies. For example, in studies comparing elderly subjects, it may be useful to choose a higher labeling location to avoid susceptibility effect of dental works.

The findings from the present study need to be interpreted in the context of its limitations. The PC velocity scan itself may contain noise due to cardiac pulsation and physiologic fluctuations, which will be propagated to the CBF map. Cardiac pulsation is particularly relevant in that flow velocity varies at different phases of the cardiac cycle and this would result in a phase-specific variation in labeling efficiency. Thus the efficiency reported in the present study can only be considered as an averaged value across all phases of the cycle, similar to the cases of CASL (Werner R et al., 2005). In addition, accurate velocity mapping at the neck regions require the RF and gradient coils to sufficiently cover the area. This was possible with our particular experimental setup. However, if the coil coverage

is not long to cover the whole brain, table movement may be needed. The pCASL technique itself has specific limitations. While the labeling pulses were designed to have lower power compared to conventional CASL, it is still greater than the PASL technique and sometimes poses limitations on labeling duration, number of slices and minimal TR. Also, the addition of extra scans to the protocol is certainly a pitfall compared to conventional ASL. The signal sensitivity to B0 and B1 inhomogeneity as well as to velocity adds further complexity to the technique.

CONCLUSION

Labeling efficiency is shown to be a critical parameter in pCASL MRI not only in terms of achieving highest sensitivity but also in quantification of absolute CBF in units of ml/min/100g. I proposed and evaluated an in vivo experimental method to estimate labeling efficiency using phase contrast MRI as a normalization factor.

SPECIFIC AIM 2: ON THE SENSITIVITY OF ASL MRI IN DETECTING REGIONAL DIFFERENCES IN CEREBRAL BLOOD FLOW

INTRODUCTION

Cerebral blood flow (CBF) is a physiological parameter reflecting blood supply to the brain and is typically written in units of ml blood per 100g tissue per min. It has been shown to be a sensitive marker for cerebrovascular diseases such as stroke, arterial stenosis, and vascular dementia (Carrera E et al., 2007; Nagata K et al., 2000; Weiss JS and BE Sumpio, 2006). Moreover, CBF measurement has played a major role in non-invasive assessment of neural activity since it can be associated with neural activity via neurovascular coupling (Roy CS and CS Sherrington, 1890; Sherrington CS, 1890). This relationship has led to the development and wide application of human brain mapping techniques using Positron Emission Tomography (PET) or functional MRI (Fox PT and ME Raichle, 1986; Ogawa S et al., 1990; Raichle ME et al., 2001). More recently, much attention was received to assess baseline neural activity between patient and control subject groups, by comparing the resting CBF values (Derejko M et al., 2001; Eisenberg DP et al., 2009; Johnson NA et al., 2005; Schuff N et al., 2009). Such applications may have great potentials in understanding disease mechanism in neurological and psychiatric disorders.

Traditionally, CBF measurement is conducted by injecting radioactively labeled tracers followed by imaging the signals using Single-Photon-Emission-Computed-Tomography (SPECT) or PET (Devous MD, Sr. *et al.*, 1986; Mintun MA et al., 1984). However, the applications of these techniques in brain disorders

are limited by the need of exogenous agent as well as the use of radioactive materials. Arterial Spin Labeling (ASL) MRI is a non-invasive technique that has the potential to provide a quantitative assessment of CBF within 5-10 minutes (Detre JA *et al.*, 1992; Edelman RR et al., 1994; Golay X et al., 2004; Kim SG, 1995; Petersen ET *et al.*, 2006; Wang J *et al.*, 2005; Williams DS *et al.*, 1992; Wong EC et al., 1997). There have been increasing numbers of studies that use ASL MRI in comparing resting CBF between patients and controls, under the assumption that CBF is a surrogate of local neural activity. However, such efforts have encountered a few difficulties, mainly because of large inter-subject variations in CBF. These variations are due to non-neural factors such as breathing pattern, physiologic state and even consumption of caffeine (Cohen ER et al., 2002; Laurienti PJ et al., 2003; Liu TT et al., 2004), which modulate CBF in a global fashion and contribute to the sources of noise in group comparison. Therefore, it is not yet clear how sensitive ASL MRI is in detecting regional neural activity differences between patients and controls and which is the best strategy to detect such differences.

In this work, I conducted experimental measurements and numerical simulation to show that raw CBF values should be normalized against CBF of the whole-brain or a reference region before conducting regional comparison. Normalization is useful for factoring out global modulation effects, thereby increasing the sensitivity of ASL MRI in detecting regional CBF differences

between two subject groups. I used a model condition in which I simulated a "patient" group by having the subjects view a flashing checkerboard and compared their CBF to that of a "control" group of subjects viewing a fixation. Group comparison was conducted on the raw CBF values (denoted as absolute CBF, aCBF) and on the CBF values normalized against whole-brain values (denoted as relative CBF_{WB}, $rCBF_{WB}$) or a central brain region (denoted as relative CBF_{CR}, $rCBF_{CR}$). In addition, numerical simulation was conducted to confirm the experimental findings and assess the ASL detection power under typical signal-to-noise-ratio (SNR).

MATERIALS AND METHODS

Experiment

Experiments were performed on a 3T MR system (Philips Medical Systems, Best, the Netherlands) using body coil transmission and head coil reception. The protocol was approved by the Institutional Review Board. A total of 14 healthy subjects (10 males, 4 females; 21-54 years of age) participated in the study after informed written consent was obtained. The subjects were divided into two groups, one group (n=7, age 28.9±12.3, 5 males, 2 females) was shown a white cross and the other group (n=7, age 29.3±7.6, 5 males, 2 females) was shown a flashing checkerboard at 4 Hz, to mimic the "control" and "patient"

groups, respectively. In addition, the "patient" group was also shown a white cross to serve as an intra-group control.

A balanced pseudo-continuous ASL (pCASL) sequence was used to measure CBF following previous studies by Wu et al. and Wong (Wong EC, 2007; Wu WC *et al.*, 2007). Imaging parameters for pCASL experiments were: single-shot gradient-echo EPI, field-of-view (FOV)=240x240, matrix=80x80, voxel size=3x3 mm^2, 27 slices acquired in ascending order, slice thickness=5 mm, no gap between slices, labeling duration=1650 ms, post labeling delay=1525 ms, TR=4020 ms, TE= 14ms, SENSE factor 2.5, time interval between consecutive slice acquisitions=35.5 ms, number of controls/labels= 30 pairs, RF duration=0.5 ms, pause between RF pulses = 0.5 ms, labeling pulse flip angle=18°, bandwidth=2.7 kHz, echo train length=35, and scan duration 4.5 min. In addition to the pCASL scan, a time-of-flight (TOF) angiogram and a phase-contrast (PC) velocity MRI were performed to obtain aCBF values following procedures established previously (Aslan S XF, Wang PL, Uh J, Yezhuvath U, van Osch M, Lu H., 2010). The TOF angiogram was performed to visualize the internal carotid arteries (ICA) and vertebral arteries (VA), and to correctly position the PC velocity MRI slice. The imaging parameters were: TR/TE/flip angle=23ms/3.45ms/18°, FOV=160x160x70 mm^3, voxel size 1.0x1.0x1.5mm^3, number of slices =47, one saturation slab of 60mm positioned above the imaging slab to suppress the venous vessels, duration 1 min 26 sec. The slice of the PC

velocity MRI was oriented perpendicular to the ICA and VA and the parameters were: single slice, voxel size=0.45x0.45 mm^2, FOV=230x230 mm^2, TR/TE=20/7 ms, flip angle=15°, slice thickness=5 mm, maximum velocity encoding=80 cm/s, and scan duration=30 sec.

A high resolution T1 weighted image was also acquired with the following parameters: MPRAGE sequence, TR/TE=8.3ms/3.8ms, flip angle=12°, 160 sagittal slices, voxel size=1x1x1 mm^3, FOV=256x256x160 mm^3, and duration 4 min.

Data Analysis

The pCASL control and label images were realigned using SPM5 (Wellcome Department of Imaging Neuroscience, London, UK) and the aCBF maps were calculated based on a procedure described previously (Aslan S XF, Wang PL, Uh J, Yezhuvath U, van Osch M, Lu H., 2010). Briefly, a difference image was calculated for each pair of the control and label images. The 30 difference images were then averaged. Slice timing correction was conducted to account for different post-labeling delay times for different brain slices. From the PC velocity MRI, the total flux in the four feeding arteries (left/right internal carotid arteries, left/right vertebral arteries) was calculated and this is the blood flow to the entire brain. The volume of the entire brain was estimated from the MPRAGE data, from which the average blood flow per unit brain mass was

calculated in units of ml/100g/min. Next, the MPRAGE brain mask was applied to the pCASL difference images and the whole-brain averaged pCASL signal (in units of MR signal) was calculated. Comparing these two averaged values, the conversion constant between pCASL MR signal and the physiologic unit was obtained and was used to calibrate the pCASL signal for individual voxels, yielding aCBF maps. The aCBF maps were spatially normalized to the brain template of Montreal Neurological Institute (MNI). Calculation of rCBF maps was based on two different normalization methods. In the first method, aCBF of each voxel was divided by the whole brain averaged aCBF, yielding a relative map $rCBF_{WB}$. In the second method, the normalization used a region that is known to be minimally affected by stimuli (or a disease) such as central region in case of visual stimulation, and yielded a map of $rCBF_{CR}$. The central brain regions contain pre- and post-central gyrus and are defined by a parcellation template in SPM (Tzourio-Mazoyer N et al., 2002).

Region-of-interest (ROI) and Voxel-based analyses (VBA) were conducted using each of the aCBF, $rCBF_{WB}$ and $rCBF_{CR}$. ROI analysis was conducted by averaging the CBF values in a region (e.g. occipital lobe) defined by a parcellation template in SPM (Tzourio-Mazoyer N *et al.*, 2002), which was then compared across the two subject groups. In VBA, the individual CBF maps were spatially smoothed (with full-width-half-maximum of 10 mm) to account for small differences in sulci/gyri location across subjects. Then I conducted Student

t-tests on each voxel in the brain. A voxel level threshold of 0.05 (False Discovery Rate, FDR, corrected) and a cluster size of 100 were used to define activated voxels. False-positive tests using randomization (Ashburner J and KJ Friston, 2000) suggested that, with this set of thresholds, the cluster level family-wise error is expected to be less than 0.05.

Signal and noise levels were calculated on a voxel-by-voxel basis as follows. For each voxel, a time course with thirty measurements was obtained from the control/label pairs. The signal level was calculated as the mean of the time course and the noise level as the standard error (i.e. standard deviation divided by $\sqrt{30}$). I then determined SNR for gray matter (GM), white matter (WM), and the whole brain. Four ROIs were drawn on eight axial slices for GM and WM, resulting in a total of 32 GM and 32 WM ROIs. Signal and noise levels were averaged across voxels in the ROIs to yield the respective average values. Their ratio was then defined as the SNR for GM (or WM). The whole brain SNR was measured by drawing an ROI around the boundary of the brain and by conducting similar calculations.

Simulation

Simulation was conducted to provide a quantitative understanding as to why CBF normalization is beneficial in detecting group differences. The

simulation also provides an assessment of the detection power under typical SNR of ASL MRI. The aCBF of a brain region can be written as:

$$aCBF(s, r, p) = g(s) \times f(r, p) + n \quad [19]$$

where $aCBF(s, r, p)$ denotes aCBF value of subject "s" in region "r" under physiologic state "p" (diseased or healthy). Conceptually, the equation can be viewed as follows. Each subject has a specific level of CBF, g(s), which is a global factor for all brain regions. Next, different regions have different levels of blood supply and this is also dependent on physiologic state. For example, CBF in frontal lobe may be 80% of the whole brain average and an individual with frontal lobe specific disease may have a CBF that is 70% of the whole brain value. Thus $f(r, p)$ is the region-specific deficit that I aim to detect with ASL MRI. Finally, the measured signal contains a noise component, n, that is assumed to be randomly distributed.

When normalizing the aCBF values with the whole brain average, g(s), the resulting $rCBF_{WB}$ can be written as:

$$rCBF_{WB}(s, r, p) = aCBF(s, r, p) / g(s) = f(r, p) + n / g(s) \quad [20]$$

Monte Carlo simulation was performed with the following parameters. Whole brain averaged CBF, g(s), was assumed to have a Gaussian distribution across individuals, with a mean value of 46 ml/100g/min and a standard deviation (SD) of 6.3 ml/100g/min (based on experimental data from a previous study

(Aslan S XF, Wang PL, Uh J, Yezhuvath U, van Osch M, Lu H., 2010)). It is assumed that the "patient" and "control" groups each contained 20 subjects. The noise term, n, was added with a Gaussian distribution of a mean of 0 and a SD based on SNR values of 2 to 10, which were typical ranges of CBF maps using ASL MRI. Regional CBF index, $f(r, p)$, was assumed to be 1 (i.e. 100%) for the "control" group and the deficit in the "patient" group varied from 10% to 60% in the simulation. The probability of detecting the group difference (using p value threshold of 0.05) was plotted as a function of SNR and true CBF difference. Each simulation was performed 50,000 times. The simulation was performed for one voxel in the brain. Under the above assumptions, the signal behavior of the other voxels is expected to follow the same detection power plot. The threshold of cluster size was not applied in the simulation as only one voxel was considered at a time. The limitation of this assumption may be detection of more voxels since the voxels are assumed to be independent from one another.

In a second simulation, the detection probability was calculated for different sample sizes and p value thresholds with other assumptions identical to the first simulation. The CBF difference between groups was assumed to be 10% and the SNR was 8.

RESULTS

Experiment

Robust CBF maps were obtained from all subjects. The SNR on a single-voxel level for white matter, gray matter, and whole brain were 0.99±0.27, 4.1±0.55, and 2.6±0.49 (mean±SD), respectively. Group average aCBF maps for fixation and flashing checkerboard groups are shown in Figure 11. ROI analysis in the occipital lobe showed that aCBF in the flashing checkerboard group was 26.0% higher compared to that of the fixation group (Table 2). The p-value was marginal (p=0.03). In contrast, the p-values using $rCBF_{WB}$ or $rCBF_{CR}$ were 10-15 times smaller (Table 2), suggesting a more sensitive comparison. Note that the percentage change observed in the $rCBF_{WB}$ comparison was actually reduced to 16.5%. This is because aCBF increase in the occipital lobe resulted in a higher whole-brain aCBF in the flashing checkerboard group (i.e. large denominator), and thus offset some of the effects in the $rCBF_{WB}$ comparison. On the other hand, when using the central region as a reference, the normalized index, $rCBF_{CR}$, showed a change (26.4%) comparable to that of aCBF.

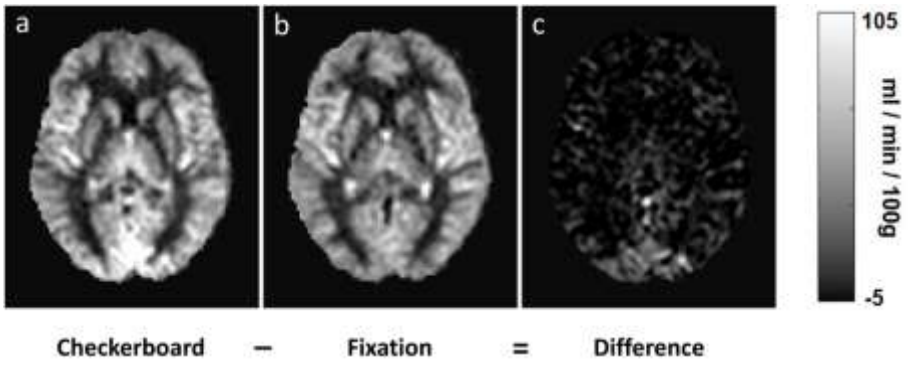

Figure 11: Averaged aCBF maps from two groups of subjects who viewed a) flashing checkerboard and b) fixation cross, respectively.

Their difference is shown in c). The aCBF maps from individual subjects were spatially normalized to the MNI brain template and then averaged. CBF increases can be seen in the occipital lobe.

Table 2: Summary of comparison of CBF maps between fixation and checkerboard groups based on various CBF indices. The last row in the table is from the VBA comparisons and the other rows are from the occipital lobe ROI comparisons.

	aCBF (ml/100g/min)	$rCBF_{WB}$ (unitless)	$rCBF_{CR}$ (unitless)
Fixation Group	49.8±3.9	1.15±0.06	1.01±0.06
Checkerboard Group	62.7±12.1	1.34±0.10	1.28±0.16
Percent Change	26.0%	16.5%	26.4%
P-value	0.03	0.002	0.003
Number of Significant Voxels	0	1619	2024

Voxel-wise comparison across groups also revealed advantages of normalization. With a threshold p-value=0.05 (False Discovery Rate (FDR) Corrected) and a cluster size of 100 voxels, comparison on aCBF data yielded no significant voxels. On the other hand, comparison on $rCBF_{WB}$ correctly identified the visual cortex as having significant differences (Figure 12a). The central-region-normalized map, $rCBF_{CR}$, yielded similar activation clusters (Figure 12b). I have also investigated the histogram of t scores of voxels in the visual cortex (Figure 13). It can be seen that the histogram shifted toward the right-hand side comparing the rCBF to aCBF results, suggesting that normalization improved statistical significance of the voxels.

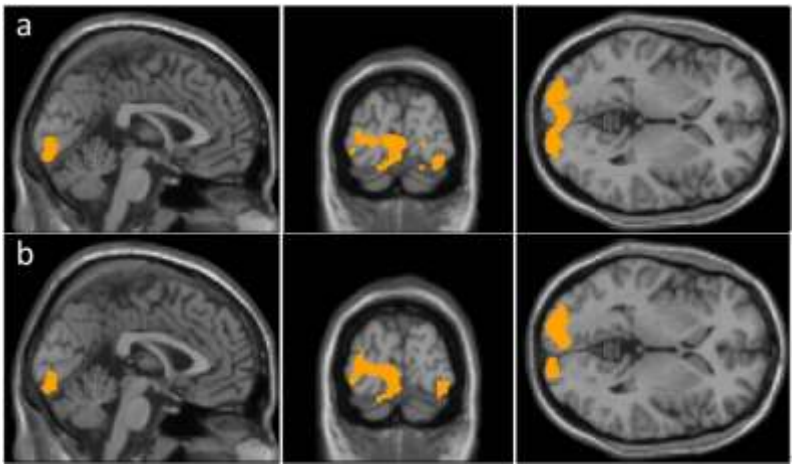

Figure 12: Results of voxel based comparison across groups using a) CBF normalized by whole brain blood flow ($rCBF_{WB}$); and b) CBF normalized by central region blood flow ($rCBF_{CR}$). The analyses were performed using an unpaired Student t-test with a threshold of $p<0.05$ (False Discovery Rate corrected) and cluster size of 100 voxels. The results of aCBF comparison were not shown because no significant cluster was detected.

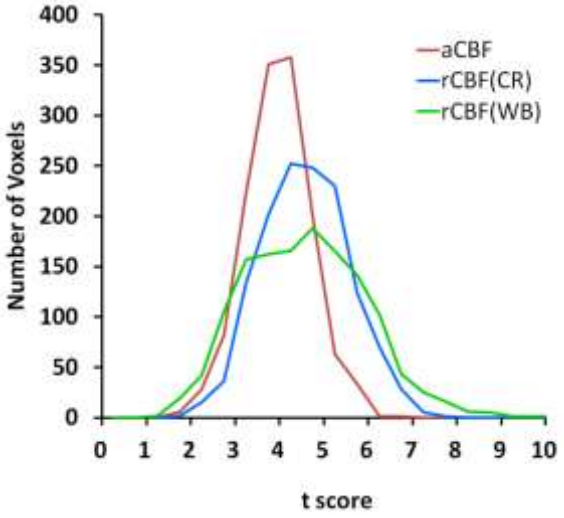

Figure 13: Histograms of t scores from individual voxels. The voxels were delineated from the intra-subject comparison of aCBF to avoid

bias in selection criteria. A total of 1375 voxels were included. The histograms shown are from inter-subject comparisons using aCBF, $rCBF_{WB}$, and $rCBF_{CR}$. Since the voxels were from the visual cortex, their t scores tend to be positive. It can be seen that the histograms of $rCBF_{WB}$ and $rCBF_{CR}$ were shifted to the right.

Similar analysis was conducted on the intra-subject comparison, in which CBF maps under the flashing checkerboard condition were compared to CBF maps under fixation condition from the SAME group of subject. Paired comparisons using aCBF maps identified visual cortices as regions with significant CBF changes (Figure 14a). Normalization with whole brain CBF or central region CBF modestly improved the activation maps (Figs. 13b and 13c). The numbers of significant voxels were 1704, 4214 and 3425 for aCBF, $rCBF_{WB}$ and $rCBF_{CR}$, respectively.

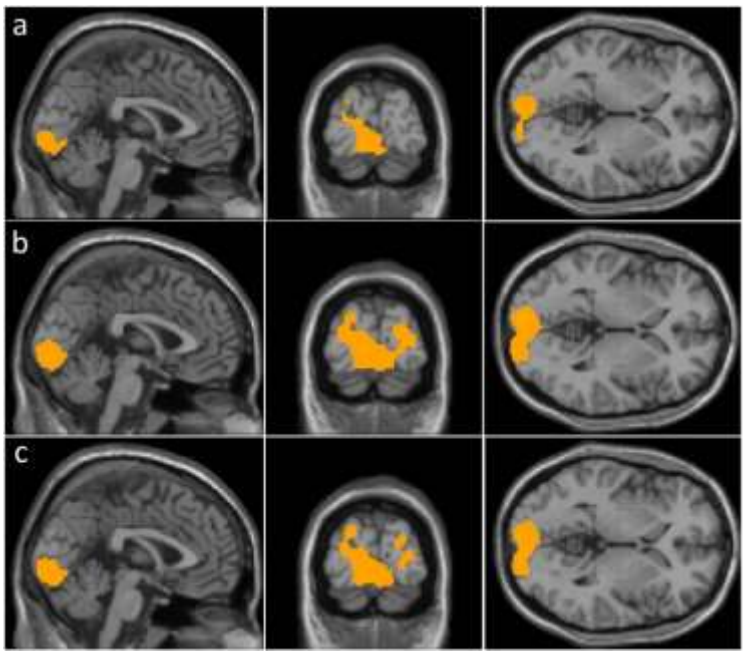

Figure 14: Results of voxel based comparison within the same group but under different conditions using a) absolute CBF (aCBF); b) CBF normalized by whole brain blood flow ($rCBF_{WB}$); and c) CBF normalized by central region blood flow ($rCBF_{CR}$). The analyses were performed using a paired Student t-test with a threshold of $p<0.05$ (False Discovery Rate corrected) and cluster size of 100 voxels.

Figure 15 shows the inter-correlation of aCBF in the frontal, parietal, temporal and occipital lobes across subjects. A significant correlation was observed for all paired comparisons ($p<0.005$). The results showed that, despite global CBF differences across subjects, regional aCBF appeared to be correlated. That is, a person with higher frontal CBF tended to have a higher CBF in the temporal, parietal and occipital lobes. Therefore, normalization of CBF as proposed above is useful in removing this global modulation.

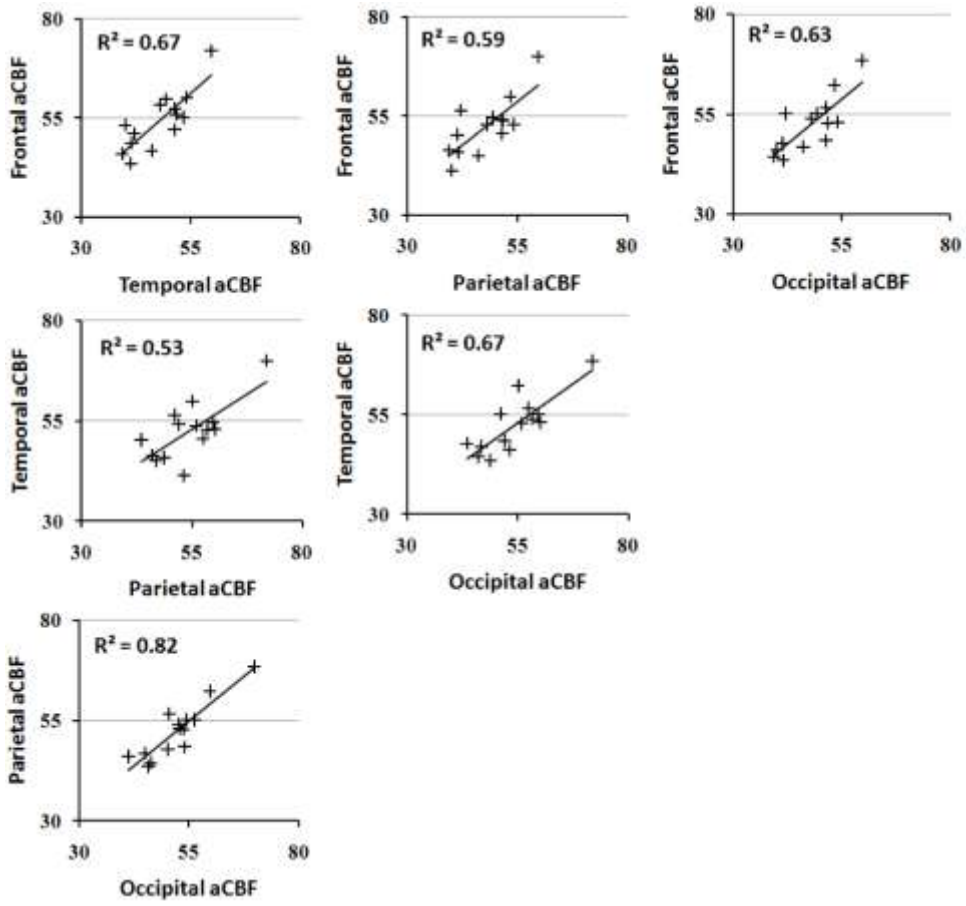

Figure 15: Scatter plots of regional aCBF values across subjects. All comparisons had a significant correlation ($p<0.005$).

Simulation

Figures 16a-b shows the probability of detection as a function of SNR and amount of CBF deficit using aCBF and rCBF, respectively. It can be seen that the rCBF plot has a higher power compared to the aCBF plot. Figure 16c shows the difference in detection power comparing aCBF and rCBF. It can be seen that the

improvement is particularly pronounced when the SNR is relatively high and the expected CBF difference is moderate.

Figures 16d-e shows the probability of detection as a function of sample size and p-value threshold. Again, rCBF showed higher power of detection compared to aCBF.

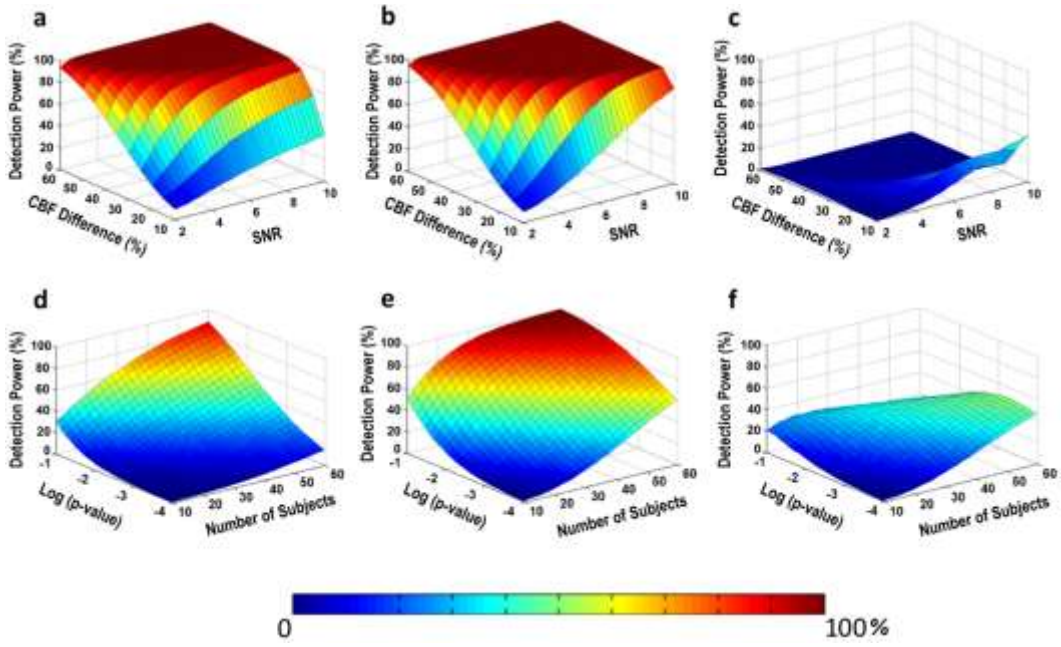

Figure 16: Results of Monte Carlo simulation for across-group comparison. Top row: Detection power as a function of SNR and CBF difference between the control and patient groups. The simulation was conducted for a) aCBF and b) rCBF. Their difference is shown in c). Bottom row: Detection power as a function of sample size and statistical threshold. Relative CBF offers a greater power in detection of group differences. The simulation was conducted for d) aCBF and e) rCBF. Their difference is shown in f).

DISCUSSION

In this study, I assessed the sensitivity of ASL MRI in detecting CBF differences across subject groups and demonstrated in a "model" situation that normalization of regional CBF using whole-brain CBF or CBF in a reference region could improve detection power. The improvement was observed in both ROI based analysis and VBA. Monte Carlo simulation confirmed the experimental findings and showed that the improvement was due to an accounting of the global variations across subjects.

ASL MRI, as a biomarker for baseline neural activity, has great potentials in clinical applications. However, questions remained as to whether ASL MRI can detect small CBF differences on the order of 10%, which is the typical range of CBF deficit occurring in many psychiatric and neurological disorders (Alsop DC et al., 2000; Dousse M et al., 1988; Lavy S et al., 1979; Theberge J, 2008). The present study provides a systematic investigation into the detection power of ASL and the optimal strategies for data analysis. I propose normalization of CBF with either global CBF or a region that is known to be unaffected by a disease. Global CBF normalization is straightforward to implement. However, this approach is applicable only when I assume that global CBF is intact, otherwise it will reduce or eliminate the CBF difference that I am seeking. Therefore, a tradeoff strategy would be to first perform a test on the global aCBF to assess whether there is a significant difference between the two groups. If no group difference in whole

brain aCBF is detected, the normalization will be applied. An alternative approach is to normalize the aCBF map with a region that is known to be unaffected by the disease or condition. In our model situation, I normalized the aCBF map with central region as visual stimulation is not expected to change blood flow in the somatosensory/motor areas. However, in some neurological or psychiatric disorders, a prior knowledge of unaffected regions may not always be available. Therefore, both of the normalization approaches have advantages and disadvantages. In our study, I observed a drastic improvement in the across-group comparison because normalization of aCBF removed the global CBF variation across subjects, which if not accounted for is a significant source of noise. The improvement in the intra-subject comparison was less pronounced because the paired test conducted for the intra-subject aCBF data uses each subject as his own control and such a test already accounted for the inter-subject variation in global CBF.

In the Monte Carlo simulation, I showed the conditions under which the improvement in detection power is most pronounced (Figure 16c). When the CBF difference is large and SNR is high, then the detection power is excellent for both aCBF and rCBF thus the normalization procedures do not provide much improvement. Similarly, when the CBF difference is small and SNR is low, everything is buried in noise and no improvement can be made. Only in the intermediate situation where CBF difference is small but SNR is relative high, the

rCBF shows a clear advantage. Interestingly, most of neuropsychiatric studies fall into this range (CBF difference between patient and control group is around 10-20%) (Alsop DC *et al.*, 2000; Dousse M *et al.*, 1988; Lavy S *et al.*, 1979; Theberge J, 2008). The gray matter SNR in our experimental data was around 4.1 on a single voxel level. With additional spatial smoothing in the group analysis (typically applied to account for small differences in sulci/gyri location across subjects), a SNR of about 8 to 10 is expected. The benefit of the proposed normalization method also relies on the assumption that the source of estimated CBF variation across subjects is primarily physiologic rather than associated with the ASL technique. I have calculated the technique-related uncertainty in individual CBF estimation and found that it is about one quarter of the variation across subjects.

The findings from the present study is consistent with a previous report by Parkes et al. who showed that a CASL scan of 6 minutes can provide reliable CBF maps with a single-voxel reproducibility (defined as 95% confidence limit) of 26% (Parkes LM et al., 2004). On the other hand, the inter-subject variation is 2-3 times greater than this value. For a ROI CBF value where many voxels are spatially averaged, the relative contribution from inter-subject variation is expected to be even greater.

CONCLUSION

ASL MRI is capable of detecting regional CBF changes across subject groups. These studies suggest that relative CBF is a more sensitive index in terms of detection power, rather than the much-sought-after absolute CBF. Relative CBF reduces physiologic noise associated with inter-subject variations in global CBF.

SPECIFIC AIM 3: ESTIMATION OF CEREBRAL BLOOD FLOW OF WHITE MATTER FIBERS IN HUMAN BRAIN

INTRODUCTION

Diffusion Tensor Imaging (DTI) MRI has become a popular technique in illustrating the anatomy of white matter fiber tracts of human brain (Basser PJ et al., 2000; Lazar M et al., 2003; Mori S et al., 1999). While this method provides useful information about underlying structural connections of brain regions and physical properties of the white matter fibers (i.e. collection of neurons' axons), it lacks the physiological properties associated with these tracts. Traditionally, anatomical imaging techniques are used to detect abnormalities in the brain; however, most neurological disorders first present themselves as physiological symptoms before anatomical changes are observed (Powers WJ et al., 1987; Sorensen AG et al., 1996). Thus, it is crucial to establish a physiological biomarker for an early diagnosis in the white matter region.

Cerebral blood flow is an important physiological biomarker reflecting blood supply to the brain and it is considered an index of neuronal activity (Roy CS and CS Sherrington, 1890; Sherrington CS, 1890). CBF is typically written in units of ml blood per 100 grams of tissue per minute and serves as an important biomarker in the detection of brain disorders (Carrera E et al., 2007; Nagata K et al., 2000). Arterial Spin Labeling MRI is a non-invasive technique that can provide CBF measurement within 5-10 minutes (Detre JA et al., 1992; Golay X et al., 2004). The ASL MRI has become the method of choice in measuring CBF compared to Dynamic Susceptibility Contrast MRI or positron emission

tomography due to its non-invasiveness, less expensive procedure, and the absence of radioactive material. One major drawback, however, with ASL MRI technique has been the white matter's low signal to noise ratio (van Gelderen P et al., 2008). This disadvantage has limited the clinical application of ASL MRI but recent technical advances, such as pseudo continuous ASL MRI and background suppression, have improved the SNR of CBF in the white matter (Garcia DM et al., 2005; van Osch MJ et al., 2009).

In this study, ten major fibers were delineated based on a previous study (Wakana S et al., 2007) and their physical properties such as fractional anisotropy (FA), which is associated with the degree of myelination in the axons, was calculated. Next, fiber specific CBF was obtained and the results showed that different fibers had different CBF. Additionally, the signal to noise ratio of each fiber and global white matter were calculated. Then, I calculated the CBF for each white matter layer of brain by erosion analysis. I found out that the CBF of white matter depends on the depth of the white matter layer. This finding, however, did not explain fiber specific difference in CBF. Further analysis of the fibers' CBF to FA showed that they were inversely correlated, suggesting that either the greater fiber myelination improves the conduction of action potential requiring less blood or restricts the blood flow to the fibers.

Recently, there has been growing interest in the relationship of structural connectivity and functional connectivity in the brain (Damoiseaux JS and MD Greicius, 2009; Greicius MD et al., 2009; Koch MA et al., 2002; Raichle ME and AZ Snyder, 2007). Functional connectivity is defined as the Pearson correlation coefficient (CC) of spontaneous fluctuation in a neural activity index between two cortical regions (Biswal B et al., 1995). As part of our study, I calculated correlation coefficient (i.e. the degree of functional connectivity) of cortical regions which are connected by white matter fibers. Previous studies chose a seed voxel and correlated the time course of the seed voxel to other brain regions but this approach may introduce a seed selection bias. In this study, however, a novel fiber based method was used to calculated CC values. First, I found the fiber terminals and then I expanded them into their neighboring cortical regions. Next, in order to accommodate for different sub-region sizes, I divided each sub-region into blocks of 10 voxels (randomly chosen) and calculated the CC value between two sub-regions. Last, I determined that the Fiber bundle's blood flows were inversely correlated with the correlation coefficient of the regions while the correlation coefficient was directly correlated with FA. These findings suggest that fibers that physically connect functionally connected regions have higher myelination; thus, the conduction of action potential becomes more efficient and the fiber does not require as much blood flow for metabolism.

MATERIALS AND METHODS

Experiment

Institutional Review Board approval was obtained for this study. A total of 10 subjects (6 males, 4 females, 25-33 years of age) were consented before participating in the study. The subjects were instructed to look at a cross (to maintain their attention) while pCASL MRI and fcMRI were performed.

Experiments were performed on a 3T MR system (Philips Medical Systems, Best, the Netherlands) using body coil transmission and head coil reception. The imaging protocol consisted of seven different MR techniques: DTI, fcMRI, T2W, pCASL, time-of-flight angiogram, phase contrast MRI, and T1W. DTI data was acquired to identify white matter fibers that connect cortical brain regions. I then performed resting state fcMRI while the subject was fixating on a cross and also a T2 weighted (T2W) scan was performed as an intermediate image for anatomic reference. I then obtained pCASL MRI followed by TOF angiogram, PC MRI, and high resolution T1W scan to estimate absolute CBF map (Aslan S et al.). The pCASL and fcMRI protocols were repeated 3 and 2 times, respectively, in order to provide sufficient SNR.

The DTI sequences were acquired using the following parameters: single-shot echo planar imaging (EPI), SENSE factor 2.5, FOV=200x200, voxel size=2.5x2.5 mm, 58 slices, slice thickness=2.5 mm, 30 directions. The fcMRI

experiment parameters included: TR=1.5s, TE=30ms, FA=60°, FOV=200x200, matrix=80x80, voxel size=2.5x2.5 mm, 29 slices, slice thickness=5 mm, no gap between slices. A T2W image was acquired with the following parameters: single-shot EPI, number of dynamics=4, TR/TE/FA=5s/59ms/90°, FOV=200x200, matrix=80x80, voxel size=2.5x2.5 mm, 58 slices, and slice thickness=2.5 mm. A balanced pCASL sequence was used following previous studies (Wong EC, 2007; Wu WC et al., 2007). PCASL protocol was acquired in two packages and the parameters were: spin-echo, FOV=200x200, matrix=80x80, voxel size=2.5x2.5 mm, 42 slices acquired in ascending order, slice thickness=2.5 mm, no gap between slices, labeling duration=1650 ms, post spin labeling delay=1525 ms, TR/TE= 4020ms/14ms, SENSE factor 2.5, time interval between consecutive slice acquisitions=54.2 ms, number of controls/labels= 30 pairs, RF duration=0.5 ms, pause between RF pulses = 0.5 ms, labeling pulse flip angle=18°, bandwidth=2.7 kHz, echo train length=35, and scan duration of 6 min. In addition to the pCASL scan, a TOF angiogram and a PC MRI were performed for calculation of aCBF (Aslan S *et al.*). The TOF angiogram was performed to visualize the internal carotid arteries and vertebral arteries, and to correctly position the PC MRI slice. The imaging parameters for TOF angiogram were: TR/TE/flip angle = 23ms/3.45ms/18°, FOV = 160x160x70 mm^3, voxel size = 1.0x1.0x1.5mm^3, number of slices = 47, one saturation slab of 60mm positioned above the imaging slab to suppress the venous vessels, duration 1 min 26 sec. The

slice of the PC MRI was oriented perpendicular to the ICA and VA and the parameters were: single slice, voxel size=0.45x0.45 mm^2, FOV=230x230 mm^2, TR/TE/FA=20ms/7ms/15°, slice thickness=5 mm, maximum velocity encoding=80 cm/s, and scan duration=30 sec. Also, a high resolution T1 weighted image was acquired with the following parameters: MPRAGE sequence, TR/TE/FA=8.3ms/3.8ms/12°, 160 sagittal slices, voxel size=1x1x1 mm^3, FOV=256x256x160 mm^3, and duration 4 min.

Data Analysis

Preprocessing of the data involved realignment of T2W images to its last dynamic (i.e. 4^{th} dynamic) and calculating the mean T2W image across four images. The averaged T2W image was segmented by using SPM2 and the white matter probability of the fiber tracts were calculated. The pCASL images were also realigned to its first image and absolute CBF map was calculated after accounting for the labeling efficiency (Aslan S et al.). Then, the mean control image of ASL and aCBF were coregistered to mean T2W image by SPM2. Ten major fibers were manually delineated in DTI Studio per previous study (Wakana S et al., 2007) and their physical properties such as FA were calculated. Then, I coregistered the fibers to T2W image via DTI B0 image. At this point, aCBF map and fiber tracts are all in the T2W image space. Finally, I applied the mask of fiber tracts to aCBF map and white matter probability map (threshold at 50%) to obtain the quantitative CBF and white matter percentage values. Furthermore, I

accounted for partial volume effect (PVE) by assuming gray matter perfusion is 2.5 times greater than white matter (Johnson NA et al., 2005; Roberts DA et al., 1994).

Absolute CBF's signal and noise levels were calculated on a voxel-by-voxel basis as follows. For each voxel of each fiber, a time course with 90 measurements was obtained from the control/label pairs. The signal level was calculated as the mean of the time course and the noise level as the standard error (i.e. standard deviation divided by $\sqrt{90}$). I then determined SNR for each fiber by averaging across voxels in the ROIs (Aslan S and H Lu). I also calculated all fibers' SNR by combining the mask of ten fiber tracts and conducted similar calculations as above.

In order to show that the aCBF of fibers are independent from their location, I classified the whole brains' white matter into different layers. To achieve this, I combined the white matter and cerebral spinal fluid (CSF) probability maps and then created a mask by thresholding the maps at 50%. I indexed the combined mask from the most outer layer (closest to cortical layer) to inner layer; ranging from 1 to 11 (some subjects had more than 11 layers). Then, the fibers' mean layer index and their aCBF for each layer was obtained. I also analyzed whole brain's white matter probability, aCBF, and FA based on the layering index. A sample image of white matter layer index is shown below.

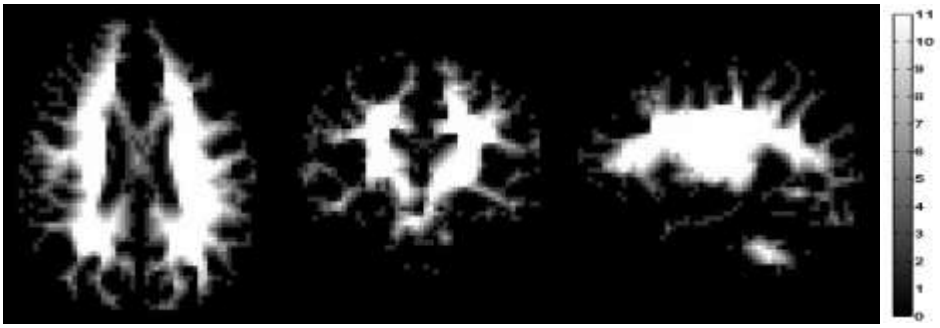

Figure 17: A sample white matter layering image is shown. The scale ranges from 0 to 11. Voxel intensity '0' signifies the voxels outside of the brain. Voxel intensity '1' is the most outer layer of white matter while voxels with intensity '11' are in the deepest layer.

The fiber approach fcMRI data analyses were performed as follows: fiber terminals were identified and expanded by three voxels (7.5 mm spherical radius) by a custom Interactive Data Language (IDL) program. These binary regions were then coregistered to T2W image via DTI B0 image and masked with gray matter probability map (threshold at 50%). Next, the regions were split into two sub-regions. For instance, the cingulum fiber terminal produced two regions: medial prefrontal cortex and posterior cingulate cortex. The two runs of fcMRI scans were realigned to the first image of the first run and their mean was calculated. Next, the fcMRI runs were coregistered to T2W image via the mean fcMRI image. In order to accommodate for sub-regions size differences, I randomly grouped the voxels in each sub-region into blocks of ten voxels. Then, the correlation coefficient between each block of each sub-region was calculated

and the average was calculated. The correlation coefficients were converted to z-score by fisher transform before averaging was conducted and then transformed back to correlation coefficient by inverse fisher transformation method.

Simulation

Simulation was conducted to provide a quantitative understanding in detecting CBF differences in fibers. The simulation also provides an assessment of the detection power under typical fiber CBF values obtained from pCASL MRI. Each simulation randomly produced 10 CBF values per fiber based on a Gaussian distribution across ten individuals where the means and standard deviations were assumed based on Table 3. Then, the power of detecting a difference between two pair of fibers (using p value threshold of 0.05) was determined. Each simulation was performed 100,000 times.

RESULTS

Table 3 summarizes the aCBF, white matter probability, fractional anisotropy values, fiber count, voxel count, layer index, and SNR of ten major fiber tracts identified manually (Wakana S *et al.*, 2007). The average CBF values of all white matter fibers were consistent with literature value, 16.1±4.8 mL/100g/min (Aslan S *et al.*; van Osch MJ *et al.*, 2009). The white matter probability of fibers were >90% which confirmed that fibers were located within

the white matter and were well coregistered to T2W image. The SNR of the fibers, shown in table 3, are clearly above noise level (SNR=1) required for blood flow quantification of fibers. The SNR of the combined white matter fibers is 0.92±0.16 which is consistent with previous studies (Aslan S and H Lu). The preceding results suggest that fibers have enough SNR to measure white matter fibers' blood flow and the difference among fibers' CBF needed further investigation. In table 4a, the blood flows of the fibers are compared (paired t-test, $p < 0.05$) across ten fibers of ten subjects. For confirmation, a Monte-Carlo simulation was conducted for ten subjects and their fibers, shown in table 4b. The findings of both experimental and simulation results were similar.

Table 3: Fiber tracts CBF (ml/min/100g), white matter probability (%), FA, fiber count, voxel count, layer index, SNR, and the correlation coefficient obtained from fiber terminals are shown (mean±stdev, n=10).

	aCBF (mL/min/ 100g)	*White Matter (%)*	*FA (unitless)*	*Fiber Count*	*Voxel Count*	*Layer Index*	*SNR*	*Correlation Coefficient*
Forceps Minor	9.7±3.9	96.0±0.6	0.52±0.02	277±108	745±196	2.96±0.16	4.42±2.21	0.27±0.16
Forceps Major	11.0±3.1	91.3±2.4	0.56±0.02	162±86	691±170	2.38±0.31	7.51±2.55	0.51±0.17
Cingulate	13.4±4.1	95.3±1.3	0.51±0.02	36±15	251±60	2.44±0.30	6.71±1.80	0.19±0.10
Inferior Fronto-Occipital Fasciculus	13.7±3.3	95.0±1.4	0.50±0.02	66±27	693±222	3.23±0.94	9.27±2.81	0.03±0.05
Inferior Longitudinal Fasciculus	14.4±3.7	94.1±1.1	0.48±0.02	112±58	754±245	2.87±0.17	9.84±3.56	0.03±0.04
Uncinate Fasciculus	16.4±6.1	91.4±1.2	0.44±1.2	128±50	370±127	2.09±0.25	7.24±3.59	0.06±0.05
Superior Longitudinal Fasciculus	16.9±2.8	96.4±1.3	0.48±0.03	54±33	386±297	4.44±0.56	10.94±2.96	0.07±0.11
Cortico-Spinal Tract	19.2±3.7	95.4±1.2	0.51±0.02	40±28	346±150	5.19±0.57	8.84±2.77	0.00±0.09
Anterior Thalamic Radiation	21.1±4.2	94.6±0.8	0.44±0.01	181±61	750±254	3.41±0.25	14.60±2.75	0.01±0.07
Hippocampal Cingulate	25.7±7.8	90.9±2.1	0.47±0.03	13±7	85±30	1.58±0.33	8.33±2.97	0.07±0.09

Table 4: a) *Experimental* results comparison (paired t-test) between different fibers' blood flow and b) *Simulation* results comparison (paired t-test) between different fibers' blood flow are shown. Both tables show similar results that with a given SNR and a blood flow value a difference between fiber perfusions can be detected. The p-values less than 0.05 are in **bold**.

a	F. Minor	F. Major	Cingulum	IFO	ILF	UNC	SLF	CS	ATR	Hippocampal Cingulate
F. Minor	1	0.41	**0.01**	**0.01**	**0.005**	**0.003**	**0.00002**	**0.0003**	**0.000003**	**0.001**
F. Major		1	0.10	**0.01**	**0.003**	**0.02**	**0.0003**	**0.000002**	**0.00005**	**0.001**
Cingulum			1	0.89	0.37	0.06	**0.006**	**0.005**	**0.000003**	**0.001**
IFO				1	0.14	0.07	**0.005**	**0.001**	**0.00001**	**0.001**
ILF					1	0.17	**0.05**	**0.005**	**0.0003**	**0.003**
UNC						1	0.76	0.25	**0.01**	**0.01**
SLF							1	0.07	**0.001**	**0.01**
CS								1	0.26	**0.05**
ATR									1	0.08
Hip. Cingulate										1

b	F. Minor	F. Major	Cingulum	IFO	ILF	UNC	SLF	CS	ATR	Hippocampal Cingulate
F. Minor	1	0.41	**0.01**	**0.01**	**0.005**	**0.003**	**0.00002**	**0.0003**	**0.0005**	**0.001**
F. Major		1	0.10	**0.01**	**0.003**	**0.02**	**0.0003**	**0.000002**	**0.0009**	**0.001**
Cingulum			1	0.89	0.37	0.06	**0.01**	**0.01**	**0.02**	**0.001**
IFO				1	0.14	0.07	**0.01**	**0.001**	**0.02**	**0.001**
ILF					1	0.17	**0.05**	**0.01**	**0.01**	**0.003**
UNC						1	0.76	0.25	**0.01**	**0.01**
SLF							1	0.07	**0.003**	**0.01**
CS								1	0.43	**0.05**
ATR									1	0.06
Hip. Cingulate										1

Figure 18a shows the number of voxels after each erosion operation (eliminating neighboring voxels in 6 directions). Figure 18b and 18c show that as I eroded ('peeled') the white matter one layer at a time from the most outer layer (i.e. closest to cortical layer), the probability of white matter and FA increased and plateau after layer four. On the other hand, the aCBF of white matter decreased for each deeper white matter layer, shown in figure 18d.

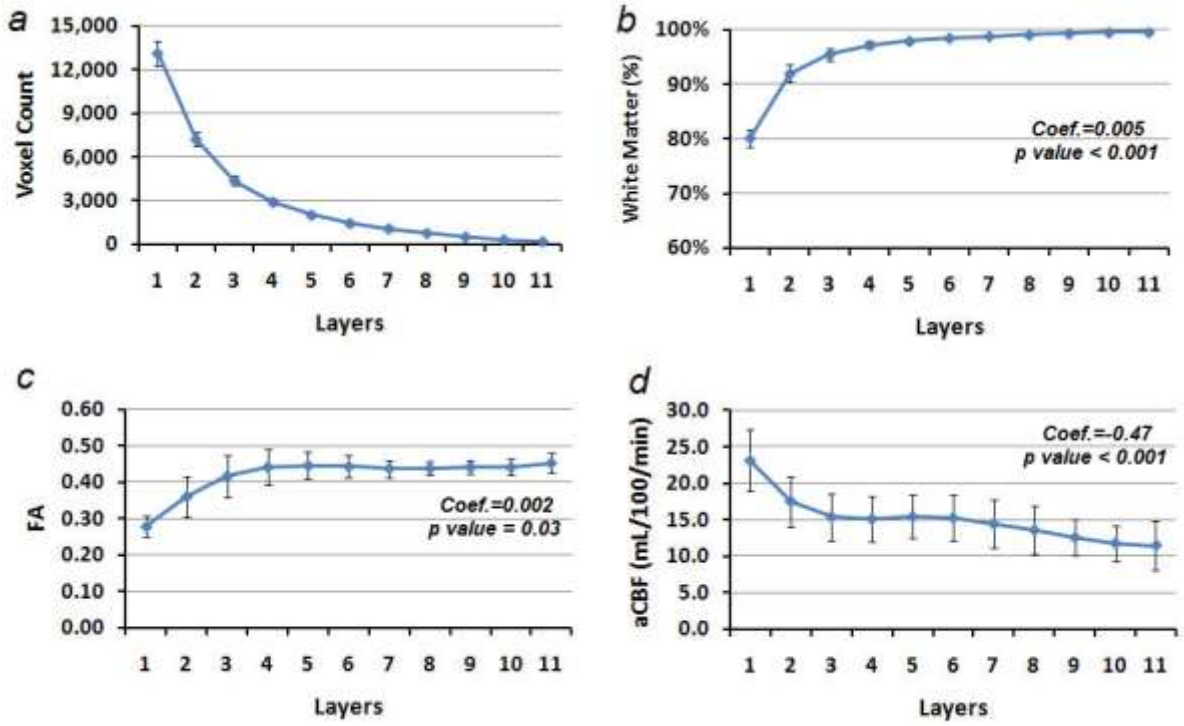

Figure 18: Erosion of global white matter for a) voxel count, b) white matter probability, c) FA and d) aCBF. As the erosion in 6 directions was conducted the white matter and FA values increased while the aCBF value decreased. The error bars depict standard deviation across subjects.

I also wanted to show that fibers are independent from their location (i.e. layering index), as there is no correlation between fibers' aCBF and their layering index (r=0.01, p=0.97), as shown in figure 19.

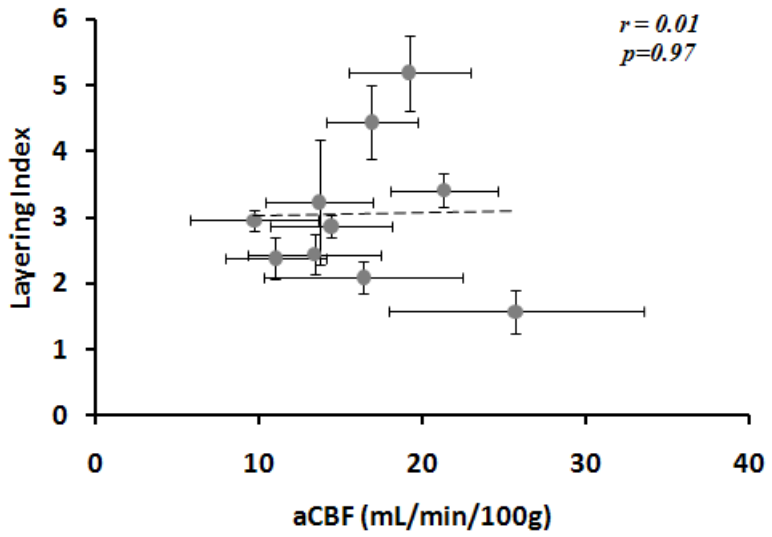

Figure 19: the fibers' blood flows are plotted against their layering index. As shown, there is no correlation between these two parameters (*r=0.01, p=0.97*).

Next, I wanted to examine if a relationship exists between the fibers' physical properties (i.e. FA) and physiological properties (i.e. aCBF). Figure 20a shows the scatter plot between aCBF and FA values of ten fiber tracts across 10 subjects (a total of 100 measurements). A strong inverse correlation was observed between FA and CBF (r = *-0.59; p=0.0001*). To further analyze this relationship, I explored CBF's relationship to radial and axial diffusivity. I found that radial diffusivity was directly correlated to CBF (r = 0.33; p = 0.004) while

the axial diffusivity was inversely correlated to CBF (*r = -0.63; p = 0.00001*), figure 20b and 20c, respectively.

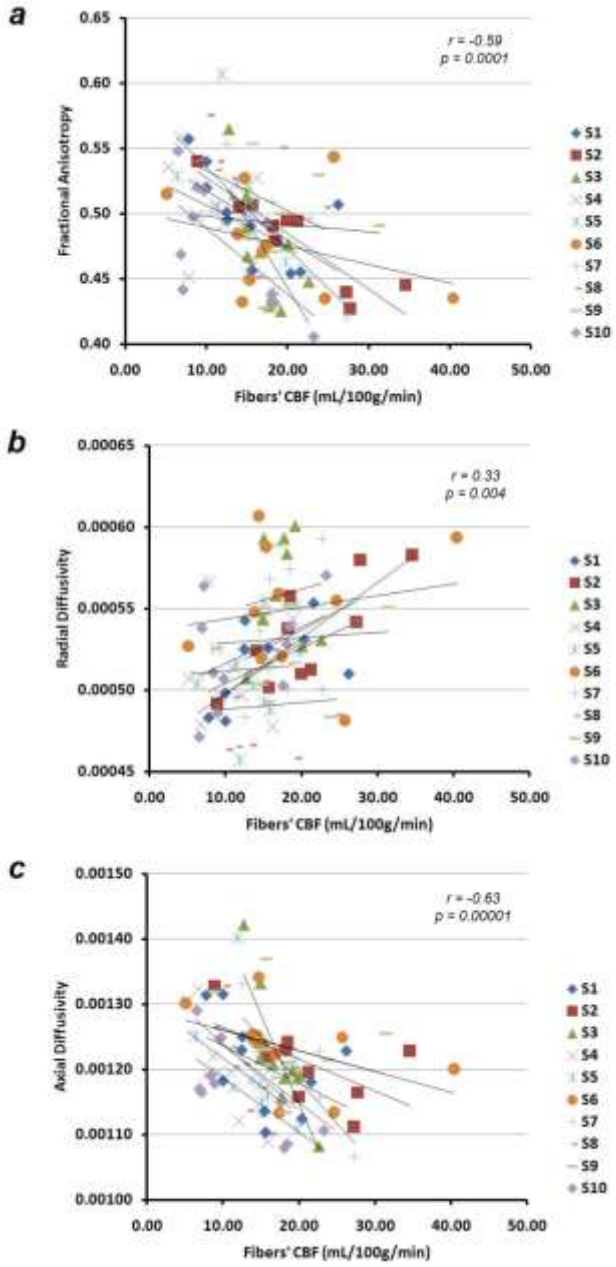

Figure 20: a) The scatter plot between aCBF and FA shows an inverse correlation while b) radial diffusivity and aCBF show direct correlation. c) aCBF and axial diffusivity are also inversely correlated. Each subject's linear trend line is also shown.

The functional connectivity results (i.e. correlation coefficient) for different regions connected by fibers are shown in table 3. The relationship between correlation coefficient of regions and FA indicated a strong correlation ($r = 0.63$; $p < 0.0001$) while regions' cross correlation and their connecting fibers' blood flow were inversely correlated ($r = -0.44$; $p = 0.0001$), shown in figure 21. These results indicated that the fibers with a higher degree of myelination (or FA) connect regions that are functionally connected. These findings indicate that a higher degree of myelination causes the action potential to conduct more efficiently along the axons; therefore, requiring less blood flow for metabolism. The correlation coefficient results also suggest that some regions which are structurally connected may not be functionally connected, such as anterior thalamic radiation regions.

The blood flow of the corpus callosum was also characterized by parceling it into four equal areas across three mid-saggital slices: genu, anterior body, posterior body, and splenium. I found a significant trend based on a linear mixed-effects model fit (*regression coefficient* = 2.2, *p=0.004*) that the blood flow increased in a stepwise fashion from anterior to posterior direction: genu=9.5

mL/min/100g, anterior body=10.2 mL/min/100g, posterior body=13.5 mL/min/100g and splenium=15.7 mL/min/100g.

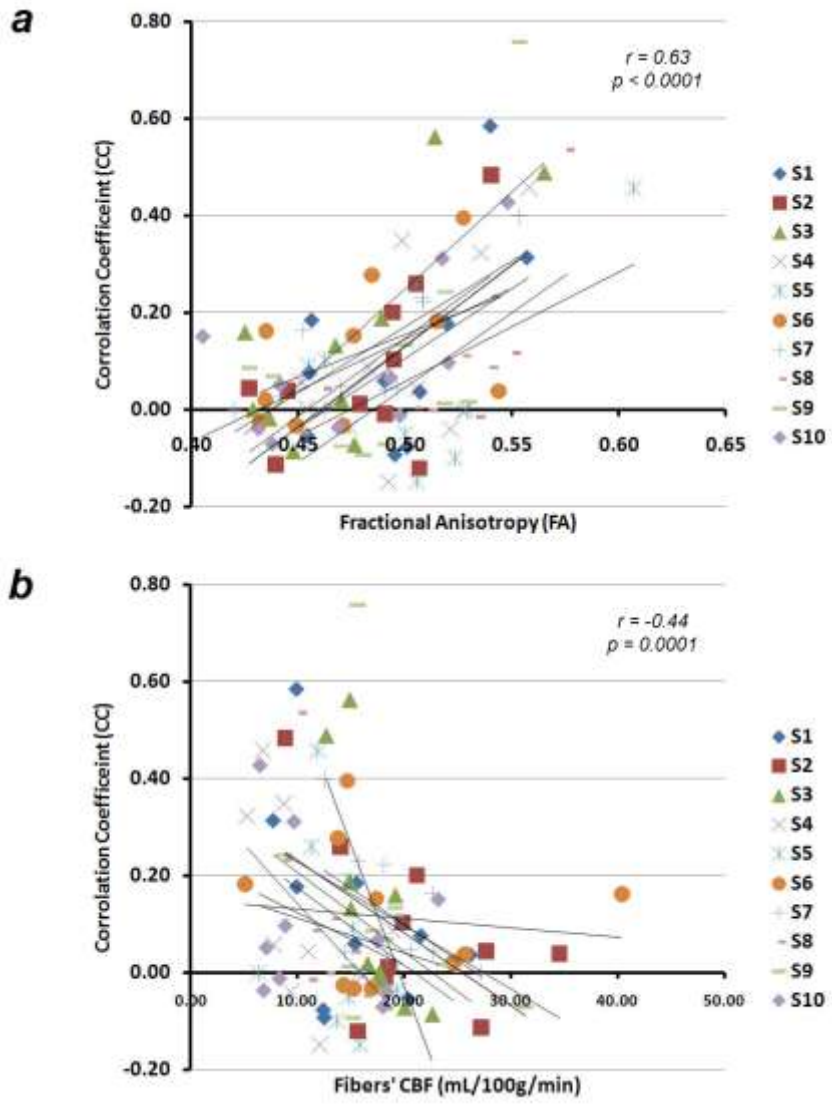

Figure 21: a) The scatter plot between cross correlation and FA shows a direct correlation while b) cross correlation and aCBF shows an inverse correlation. Each subject's linear trend line is also shown.

DISCUSSION

In this study, I estimated aCBF value of ten major fibers for the first time in the human brain. The estimation of aCBF was calculated by combining PC MRI and pCASL MRI (Aslan S *et al.*) while the white matter fibers were delineated by DTI MRI in DTI Studio (Wakana S *et al.*, 2007). All defined fibers had a high white matter probability (> 90%) and their average aCBF values were consistent with white matter aCBF values reported in the current literature. This quantification has established a physiologically meaningful parameter for brain fibers, i.e. aCBF in terms of mL/min/100g, and may help in the characterization of neurologic and psychiatric disorders.

Each Fiber had a particular blood flow and I showed that this difference was not due to their location or the depth of fibers in the brain. However, I observed that the white matter layers close to the cortical regions had higher blood flow compared to deeper white matter layers. This finding is consistent with Duvernoy et al. in that the capillaries became less dense in the deep white matter regions (Duvernoy HM et al., 1981). While blood flow of the white matter changed across layers, the fibers' blood flow did not show any significant correlation to their layering index.

I also explored the relationship between aCBF and FA. Fractional anisotropy is a physical property of fibers that is typically known for the degree of

myelination in the axons while CBF is a neuronal activity index. I observed an inverse correlation between aCBF and FA, suggesting that higher myelination leads to lower blood flow. There are two possible speculations for this phenomenon: 1. Higher myelination restricted the blood flow to the center of the fiber or 2. Higher myelination made the conductance of the action potential more efficient; thus, the fiber did not require as much blood flow for glucose and oxygen consumption. To further analyze this relationship, I also evaluated axial and radial diffusivity. A direct correlation between radial diffusivity and CBF suggests that increased radial diffusivity requires a higher blood flow and reflected a less efficient fiber structure. Our finding was consistent with Song et al. in that demyelination caused by injury increased radial diffusivity (Song SK et al., 2005). On the other hand, axial diffusivity was inversely correlated to CBF suggesting that higher myelination sheath layers required less blood flow for the fiber.

Understanding resting brain via fcMRI has become the topic of interest in recent years. A few recent studies have found that some brain regions are both functionally and structurally connected. Although these studies have widened the understanding of resting state brain, they have not provided an insight into white matter connections *in action.* Here, I used white matter fibers to find brain regions connected and calculated their correlation coefficient. Our finding indicates that regions which are functionally connected require less blood flow in

their structural connection. This may be due to higher degree of myelination in the fibers which supports our second assumption of efficient action potential conduction.

CONCLUSION

ASL MRI is capable of measuring CBF in white matter fibers. The functional connectivity of the regions that are structurally connected could affect the myelination (fractional anisotropy) and the blood flow of these fibers. The white matter fibers' FA is inversely correlated to fibers' CBF ($r = -0.59$; $p=0.0001$). This study has provided an index for white matter fibers' blood flow that could possibly be used in diagnosis of neurological disorders before anatomical change is observed.

ACKNOWLEDGEMENTS

This study was supported in part by the VA IDIQ contract number VA549-P-0027 awarded and administered by the Dallas, TX VA Medical Center. The content of this paper does not necessarily reflect the position or the policy of the U.S. government, and no official endorsement should be inferred.

Appendix A

Bloch equation describes the net magnetization of a spin system changes over time in the presence of a time-varying magnetic field.

$$\frac{d\vec{M}}{dt} = \underbrace{\gamma\vec{M} \times \vec{B}}_{\text{Precession Term}} + \underbrace{\frac{1}{T_1}\left(\vec{M}_0 - \vec{M}_z\right)}_{\text{T1 Term}} - \underbrace{\frac{1}{T_2}\left(\vec{M}_x + \vec{M}_y\right)}_{\text{T2 Term}} \quad [1]$$

Two time constants, called T1 and T2. T1 for the re-growth of longitudinal magnetization, and T2 decay of the transverse component (Mx and My). Since pCASL MRI depends on T1 relaxation, below is the dependence of T1 term on the blood flow.

$$\frac{dM_z(t)}{dt} = \underbrace{\frac{1}{T_{1,b}}\left(M_b^o - M_b(t)\right)}_{\substack{\text{T1 Term} \\ \text{z-magnetization}}} + \underbrace{fM_a(t)}_{\text{Arterial}} - \underbrace{fM_v(t)}_{\text{Venous}} \quad [2]$$

Under fully relaxed conditions, the magnetization of brain water and arterial blood (no inversion) are equal, $M_a(t) = M_b^o/\lambda$.

Magnetization of spins in the venous outflow is equal to brain tissue $M_v(t) = M_b(t)/\lambda$.

So the equation become

$$\frac{dM_z(t)}{dt} = \frac{1}{T_{1,b}}\left(M_b^o - M_b(t)\right) + f/\lambda\, M_b^o - \frac{f}{\lambda} M_b(t) \qquad [3]$$

After solving the equation I get

$$\frac{d\left(M_b(t) - M_b^0\right)}{dt} = -\left(M_b(t) - M_b^0\right)\left(\frac{1}{T_{1app}}\right) \qquad [4]$$

Where T_{1app} is given by:

$$\left(\frac{1}{T_1} + \frac{f}{\lambda}\right) = \frac{1}{T_{1app}} \qquad [5]$$

For *Control image*:

The equation 4 can be solved by differential equation similar to

$$M(t) = Ce^{-t/T_1}$$

If I replace the term 'C' with ' $-\left(M_b(t) - M_b^0\right)$', then the equation will become

$$M_b(t) - M_b^0 = C \cdot e^{-t/T_{1app}} \qquad [6]$$

For t=0, the equation becomes

$$M_b(0) - M_b^0 = C$$

And for C=0, the Control image of pCASL become:

$$M_b(0) = M_b^0 \quad [7]$$

For the *Labeled image*:

At the labeling slab the spins magnetization is $M_a(t) = M_a^0$.

Once leaving labeling slab and traveling to the imaging slab, spins undergo T1 decay at the imaging slab, $M_a(t) = M_a^0\left(1 - 2\alpha e^{-\frac{t}{T_{1,a}}}\right)$, α is the labeling efficiency.

$$M_a(t) = M_a^0\left(1 - 2\alpha e^{-\frac{t}{T_{1,a}}}\right) = \frac{M_b^0}{\lambda}\left(1 - 2\alpha e^{-\frac{t}{T_{1,a}}}\right) \quad [8]$$

Transit time from labeling slice to the voxel being imaged is δ.

If continuously labeled, at the imaging voxel:

$$M_a = M_a(\delta) = \frac{M_b^0}{\lambda}\left(1 - 2\alpha e^{-\frac{\delta}{T_{1,a}}}\right) \quad [9]$$

$$\frac{dM_b(t)}{dt} = \frac{\left(M_b^0 - M_b(t)\right)}{\lambda} + \frac{f}{\lambda}M_b^0\left(1 - 2\alpha e^{-\frac{\delta}{T_{1,a}}}\right) - \frac{f}{\lambda}M_b(t) \quad [10]$$

$$\frac{d\left(M_b^0 - M_b(t) - T_{1app}\cdot 2\alpha\frac{f}{\lambda}M_b^0\cdot e^{-\frac{\delta}{T_{1a}}}\right)}{dt} = -\frac{M_b^0 - M_b(t) - T_{1app}\cdot 2\alpha\frac{f}{\lambda}M_b^0\cdot e^{-\frac{\delta}{T_{1a}}}}{T_{1app}} \quad [11]$$

$$M_b^0 - M_b(t) - T_{1app}\cdot 2\alpha\frac{f}{\lambda}M_b^0\cdot e^{-\frac{\delta}{T_{1a}}} = C\cdot e^{-\frac{t}{T_{1app}}} \quad [12]$$

$$M_b(0) = M_b^0$$

Bringing in the initial condition

$$M_b^0 - M_b(t = 0) - T_{1app} \cdot 2\alpha \frac{f}{\lambda} M_b^0 \cdot e^{-\frac{\delta}{T_{1a}}} = C \quad [13]$$

$$C = -T_{1app} \cdot 2\alpha \frac{f}{\lambda} M_b^0 \cdot e^{-\frac{\delta}{T_{1a}}} \quad [14]$$

$$M_b^0 - M_b(t) = T_{1app} \cdot 2\alpha \frac{f}{\lambda} M_b^0 \cdot e^{-\frac{\delta}{T_{1a}}} \left(1 - e^{-\frac{\delta}{T_{1app}}}\right) \quad [15]$$

So for steady state, $t \to \infty$, $1 - e^{-\frac{t}{T_{1app}}}$, it become 1.

$$M_b^0 - M_b^{ss} = T_{1app} \cdot 2\alpha \frac{f}{\lambda} M_b^0 \cdot e^{-\frac{\delta}{T_{1a}}} \quad [16]$$

$$\because M_{b,control}^0 = M_b^0 \quad [17]$$

$$\because M_{b,control}^0 - M_{b,label}^0 = T_{1app} \cdot 2\alpha \frac{f}{\lambda} M_b^0 \cdot e^{-\frac{\delta}{T_{1a}}} \quad [18]$$

For pCASL, assume waiting time = w.

1) If $w \leq \delta$, the imaging voxel is still at its steady state,

   So with continuous labeling:

$$M_{b,control}^0 - M_{b,label}^{ss} = T_{1app} \cdot 2\alpha \frac{f}{\lambda} M_b^0 \cdot e^{-\frac{\delta}{T_{1a}}} \quad [19]$$

2) If $w > \delta$, $M_a(t) = M_a^0$, the newly arrived spins are not inverted:

$$\frac{dM_b^0}{dt} = \frac{1}{T_{1b}}\left(M_b^0 - M_b(t)\right) + \frac{f}{\lambda} M_b^0 - \frac{f}{\lambda} M_b(t) \quad [20]$$

   Since $M_a^0 = \frac{M_b^0}{\lambda}$ then

$M_b^0 - M_b(t) = C \cdot e^{-\frac{t}{T_{1app}}}$, where $t = w - \delta$.

The initial condition t = w – δ = 0 is $M_b\left(t = 0\right) = M_b^{ss}$, previously steady state.

$$M_b^0 - M_b^{ss} = T_{1app} \cdot 2\alpha \frac{f}{\lambda} M_b^0 e^{-\frac{\delta}{T_{1a}}} \quad [21]$$

So, $M_b^0 - M_b\left(t\right) = T_{1app} \cdot 2\alpha \frac{f}{\lambda} M_b^0 e^{-\frac{\delta}{T_{1a}}} \cdot e^{-\frac{t}{T_{1app}}}$

$$M_{b,control} - M_{b,label}\left(w - \delta\right) = T_{1app} \cdot 2\alpha \frac{f}{\lambda} M_b^0 e^{-\frac{\delta}{T_{1a}}} \cdot e^{-\frac{w-\delta}{T_{1app}}} \quad [22]$$

Since

$$e^{-\frac{\min\left(\delta - w, 0\right)}{T_{1app}}} = e^{-\frac{\max\left(w-\delta, 0\right)}{T_{1app}}} = \begin{cases} 1, w \le \delta \\ e^{-\frac{w-\delta}{T_{1app}}}, w > \delta \end{cases} \quad [23]$$

Combine 1 and 2:

$$M_{b,control} - M_{b,label}\left(w - \delta\right) = T_{1app} \cdot 2\alpha \frac{f}{\lambda} M_b^0 e^{-\frac{\delta}{T_{1a}}} \cdot e^{-\frac{\min\left(w-\delta, 0\right)}{T_{1app}}} \quad [24]$$

The labeling image for (w > δ) with transit delay and imaging delay becomes

$$M_{b,control}^{ss} - M_{b,label}^{ss}\left(w - \delta\right) = T_{1app} \cdot 2\alpha \frac{f}{\lambda} M_b^0 e^{-\frac{\delta}{T_{1a}}} \cdot e^{\frac{\delta - w}{T_{1app}}} \quad [25]$$

REFERENCES

Alsop DC, Detre JA (1996) Reduced transit-time sensitivity in noninvasive magnetic resonance imaging of human cerebral blood flow. J Cereb Blood Flow Metab 16: 1236-1249.

Alsop DC, Detre JA, Grossman M (2000) Assessment of cerebral blood flow in Alzheimer's disease by spin-labeled magnetic resonance imaging. Ann Neurol 47: 93-100.

Ashburner J, Friston KJ (2000) Voxel-based morphometry--the methods. Neuroimage 11: 805-821.

Aslan S, Lu H On the sensitivity of ASL MRI in detecting regional differences in cerebral blood flow. Magn Reson Imaging 28: 928-935.

Aslan S XF, Wang PL, Uh J, Yezhuvath U, van Osch M, Lu H. (2010) Estimation of Labeling Efficiency in pseudo-Continuous Arterial Spin Labeling. Magn Reson Med: In Press.

Aslan S, Xu F, Wang PL, Uh J, Yezhuvath US, van Osch M, Lu H Estimation of labeling efficiency in pseudocontinuous arterial spin labeling. Magn Reson Med 63: 765-771.

Austin G, Laffin D, Hayward W (1975) Cerebral blood flow in patients undergoing microanastomosis for modification for prevention of stroke. Ann Clin Lab Sci 5: 229-235.

Basser PJ, Pajevic S, Pierpaoli C, Duda J, Aldroubi A (2000) In vivo fiber tractography using DT-MRI data. Magn Reson Med 44: 625-632.

Baxter LR, Jr., Mazziotta JC, Phelps ME, Selin CE, Guze BH, Fairbanks L (1987) Cerebral glucose metabolic rates in normal human females versus normal males. Psychiatry Res 21: 237-245.

Bell BA (1984) A history of the study of the cerebral circulation and the measurement of cerebral blood flow. Neurosurgery 14: 238-246.

Biswal B, Yetkin FZ, Haughton VM, Hyde JS (1995) Functional connectivity in the motor cortex of resting human brain using echo-planar MRI. Magn Reson Med 34: 537-541.

Carrera E, Maeder-Ingvar M, Rossetti AO, Devuyst G, Bogousslavsky J (2007) Trends in risk factors, patterns and causes in hospitalized strokes over 25 years: The Lausanne Stroke Registry. Cerebrovasc Dis 24: 97-103.

Cohen ER, Ugurbil K, Kim SG (2002) Effect of basal conditions on the magnitude and dynamics of the blood oxygenation level-dependent fMRI response. J Cereb Blood Flow Metab 22: 1042-1053.

Dai W, Garcia D, de Bazelaire C, Alsop DC (2008) Continuous flow-driven inversion for arterial spin labeling using pulsed radio frequency and gradient fields. Magn Reson Med 60: 1488-1497.

Damoiseaux JS, Greicius MD (2009) Greater than the sum of its parts: a review of studies combining structural connectivity and resting-state functional connectivity. Brain Struct Funct 213: 525-533.

Daniel DG, Mathew RJ, Wilson WH (1989) Sex roles and regional cerebral blood flow. Psychiatry Res 27: 55-64.

Derejko M, Slawek J, Lass P, Nyka WM (2001) Cerebral blood flow changes in Parkinson?s disease associated with dementia. Nucl Med Rev Cent East Eur 4: 123-127.

Detre JA, Alsop DC (1999) Perfusion magnetic resonance imaging with continuous arterial spin labeling: methods and clinical applications in the central nervous system. Eur J Radiol 30: 115-124.

Detre JA, Leigh JS, Williams DS, Koretsky AP (1992) Perfusion imaging. Magn Reson Med 23: 37-45.

Devous MD, Sr., Stokely EM, Chehabi HH, Bonte FJ (1986) Normal distribution of regional cerebral blood flow measured by dynamic single-photon emission tomography. J Cereb Blood Flow Metab 6: 95-104.

Dousse M, Mamo H, Ponsin JC, Tran Dinh Y (1988) Cerebral blood flow in schizophrenia. Exp Neurol 100: 98-111.

Duvernoy HM, Delon S, Vannson JL (1981) Cortical blood vessels of the human brain. Brain Res Bull 7: 519-579.

Edelman RR, Siewert B, Darby DG, Thangaraj V, Nobre AC, Mesulam MM, Warach S (1994) Qualitative mapping of cerebral blood flow and functional localization with echo-planar MR imaging and signal targeting with alternating radio frequency. Radiology 192: 513-520.

Eisenberg DP, Sarpal D, Kohn PD, Meyer-Lindenberg A, Wint D, Kolachana B, Apud J, Weinberger DR, Berman KF (2009) Catechol-O-Methyltransferase Valine(158)Methionine Genotype and Resting Regional Cerebral Blood Flow in Medication-Free Patients with Schizophrenia. Biol Psychiatry.

Fernandez-Seara MA, Edlow BL, Hoang A, Wang J, Feinberg DA, Detre JA (2008) Minimizing acquisition time of arterial spin labeling at 3T. Magn Reson Med 59: 1467-1471.

Fox PT, Raichle ME (1986) Focal physiological uncoupling of cerebral blood flow and oxidative metabolism during somatosensory stimulation in human subjects. Proc Natl Acad Sci U S A 83: 1140-1144.

Garcia DM dBC, Alsop DC (2005) Pseudo-continuous flow driven adiabatic inversion for arterial spin lableing. In: Proceedings of the 13th Annual Meeting of ISMRM, Miami Beach, FL, USA: (Abstract 9).

Garcia DM, Duhamel G, Alsop DC (2005) Efficiency of inversion pulses for background suppressed arterial spin labeling. Magn Reson Med 54: 366-372.

Golay X, Hendrikse J, Lim TC (2004) Perfusion imaging using arterial spin labeling. Top Magn Reson Imaging 15: 10-27.

Golay X, Stuber M, Pruessmann KP, Meier D, Boesiger P (1999) Transfer insensitive labeling technique (TILT): application to multislice functional perfusion imaging. J Magn Reson Imaging 9: 454-461.

Gray H (1988) Gray's Anatomy: Gramercy.

Greicius MD, Supekar K, Menon V, Dougherty RF (2009) Resting-state functional connectivity reflects structural connectivity in the default mode network. Cereb Cortex 19: 72-78.

Grubb RL, Jr., Raichle ME, Eichling JO, Ter-Pogossian MM (1974) The effects of changes in PaCO2 on cerebral blood volume, blood flow, and vascular mean transit time. Stroke 5: 630-639.

Gunther M, Oshio K, Feinberg DA (2005) Single-shot 3D imaging techniques improve arterial spin labeling perfusion measurements. Magn Reson Med 54: 491-498.

Haacke EM BR, Thompson MR, Venkatesan R (1999) Magnetic Resonance Imaging: Physical Principles and Sequence Design: Wiley-Liss.

Hendrikse J, Lu H, van der Grond J, Van Zijl PC, Golay X (2003) Measurements of cerebral perfusion and arterial hemodynamics during visual stimulation using TURBO-TILT. Magn Reson Med 50: 429-433.

Herscovitch P, Raichle ME (1985) What is the correct value for the brain--blood partition coefficient for water? J Cereb Blood Flow Metab 5: 65-69.

Johnson NA, Jahng GH, Weiner MW, Miller BL, Chui HC, Jagust WJ, Gorno-Tempini ML, Schuff N (2005) Pattern of cerebral hypoperfusion in Alzheimer disease and mild cognitive impairment measured with arterial spin-labeling MR imaging: initial experience. Radiology 234: 851-859.

Kety SS (1951) The theory and applications of the exchange of inert gas at the lungs and tissues. Pharmacol Rev 3: 1-41.

Kety SS, Schmidt CF (1948) The Nitrous Oxide Method for the Quantitative Determination of Cerebral Blood Flow in Man: Theory, Procedure and Normal Values. J Clin Invest 27: 476-483.

Kim SG (1995) Quantification of relative cerebral blood flow change by flow-sensitive alternating inversion recovery (FAIR) technique: application to functional mapping. Magn Reson Med 34: 293-301.

Koch MA, Norris DG, Hund-Georgiadis M (2002) An investigation of functional and anatomical connectivity using magnetic resonance imaging. Neuroimage 16: 241-250.

Kwong KK, Chesler DA, Weisskoff RM, Donahue KM, Davis TL, Ostergaard L, Campbell TA, Rosen BR (1995) MR perfusion studies with T1-weighted echo planar imaging. Magn Reson Med 34: 878-887.

Laniado M, Weinmann HJ, Schorner W, Felix R, Speck U (1984) First use of GdDTPA/dimeglumine in man. Physiol Chem Phys Med NMR 16: 157-165.

Laurienti PJ, Field AS, Burdette JH, Maldjian JA, Yen YF, Moody DM (2003) Relationship between caffeine-induced changes in resting cerebral perfusion and blood oxygenation level-dependent signal. AJNR Am J Neuroradiol 24: 1607-1611.

Lauterbur PC (1989) Image formation by induced local interactions. Examples employing nuclear magnetic resonance. 1973. Clin Orthop Relat Res: 3-6.

Lavy S, Melamed E, Cooper G, Bentin S, Rinot Y (1979) Regional cerebral blood flow in patients with Parkinson's disease. Arch Neurol 36: 344-348.

Lazar M, Weinstein DM, Tsuruda JS, Hasan KM, Arfanakis K, Meyerand ME, Badie B, Rowley HA, Haughton V, Field A, Alexander AL (2003) White matter tractography using diffusion tensor deflection. Hum Brain Mapp 18: 306-321.

Leenders KL (1994) PET: blood flow and oxygen consumption in brain tumors. J Neurooncol 22: 269-273.

Leenders KL, Perani D, Lammertsma AA, Heather JD, Buckingham P, Healy MJ, Gibbs JM, Wise RJ, Hatazawa J, Herold S, et al. (1990) Cerebral blood flow, blood volume and oxygen utilization. Normal values and effect of age. Brain 113 (Pt 1): 27-47.

Liu TT, Behzadi Y, Restom K, Uludag K, Lu K, Buracas GT, Dubowitz DJ, Buxton RB (2004) Caffeine alters the temporal dynamics of the visual BOLD response. Neuroimage 23: 1402-1413.

Lu H, Clingman C, Golay X, van Zijl PC (2004) Determining the longitudinal relaxation time (T1) of blood at 3.0 Tesla. Magn Reson Med 52: 679-682.

Lu H, Nagae-Poetscher LM, Golay X, Lin D, Pomper M, van Zijl PC (2005) Routine clinical brain MRI sequences for use at 3.0 Tesla. J Magn Reson Imaging 22: 13-22.

Maccotta L, Detre JA, Alsop DC (1997) The efficiency of adiabatic inversion for perfusion imaging by arterial spin labeling. NMR Biomed 10: 216-221.

Mintun MA, Raichle ME, Martin WR, Herscovitch P (1984) Brain oxygen utilization measured with O-15 radiotracers and positron emission tomography. J Nucl Med 25: 177-187.

Mori S, Crain BJ, Chacko VP, van Zijl PC (1999) Three-dimensional tracking of axonal projections in the brain by magnetic resonance imaging. Ann Neurol 45: 265-269.

Nagata K, Maruya H, Yuya H, Terashi H, Mito Y, Kato H, Sato M, Satoh Y, Watahiki Y, Hirata Y, Yokoyama E, Hatazawa J (2000) Can PET data differentiate Alzheimer's disease from vascular dementia? Ann N Y Acad Sci 903: 252-261.

O'Gorman RL, Summers PE, Zelaya FO, Williams SC, Alsop DC, Lythgoe DJ (2006) In vivo estimation of the flow-driven adiabatic inversion efficiency for continuous arterial spin labeling: a method using phase contrast magnetic resonance angiography. Magn Reson Med 55: 1291-1297.

Ogawa S, Lee TM, Kay AR, Tank DW (1990) Brain magnetic resonance imaging with contrast dependent on blood oxygenation. Proc Natl Acad Sci U S A 87: 9868-9872.

Oguz KK, Golay X, Pizzini FB, Freer CA, Winrow N, Ichord R, Casella JF, van Zijl PC, Melhem ER (2003) Sickle cell disease: continuous arterial spin-labeling perfusion MR imaging in children. Radiology 227: 567-574.

Ostergaard L, Sorensen AG, Kwong KK, Weisskoff RM, Gyldensted C, Rosen BR (1996) High resolution measurement of cerebral blood flow using intravascular tracer bolus passages. Part II: Experimental comparison and preliminary results. Magn Reson Med 36: 726-736.

Ostergaard L, Weisskoff RM, Chesler DA, Gyldensted C, Rosen BR (1996) High resolution measurement of cerebral blood flow using intravascular tracer bolus passages. Part I: Mathematical approach and statistical analysis. Magn Reson Med 36: 715-725.

Ott R (1994) PET and SPECT Functional Imaging. In: The Institution of Electrical Engineers. London, UK: IEE. pp 1-2.

Parkes LM, Rashid W, Chard DT, Tofts PS (2004) Normal cerebral perfusion measurements using arterial spin labeling: reproducibility, stability, and age and gender effects. Magn Reson Med 51: 736-743.

Petersen ET, Lim T, Golay X (2006) Model-free arterial spin labeling quantification approach for perfusion MRI. Magn Reson Med 55: 219-232.

Powers WJ, Press GA, Grubb RL, Jr., Gado M, Raichle ME (1987) The effect of hemodynamically significant carotid artery disease on the hemodynamic status of the cerebral circulation. Ann Intern Med 106: 27-34.

Raichle ME, MacLeod AM, Snyder AZ, Powers WJ, Gusnard DA, Shulman GL (2001) A default mode of brain function. Proc Natl Acad Sci U S A 98: 676-682.

Raichle ME, Snyder AZ (2007) A default mode of brain function: a brief history of an evolving idea. Neuroimage 37: 1083-1090; discussion 1097-1089.

Rempp KA, Brix G, Wenz F, Becker CR, Guckel F, Lorenz WJ (1994) Quantification of regional cerebral blood flow and volume with dynamic susceptibility contrast-enhanced MR imaging. Radiology 193: 637-641.

Roberts DA, Detre JA, Bolinger L, Insko EK, Leigh JS, Jr. (1994) Quantitative magnetic resonance imaging of human brain perfusion at 1.5 T using steady-state inversion of arterial water. Proc Natl Acad Sci U S A 91: 33-37.

Rosen BR, Belliveau JW, Vevea JM, Brady TJ (1990) Perfusion imaging with NMR contrast agents. Magn Reson Med 14: 249-265.

Roy CS, Sherrington CS (1890) On the Regulation of the Blood-supply of the Brain. J Physiol 11: 85-158 117.

Schuff N, Matsumoto S, Kmiecik J, Studholme C, Du A, Ezekiel F, Miller BL, Kramer JH, Jagust WJ, Chui HC, Weiner MW (2009) Cerebral blood flow in ischemic vascular dementia and Alzheimer's disease, measured by arterial spin-labeling magnetic resonance imaging. Alzheimers Dement 5: 454-462.

Sherrington CS (1890) Further Note on Degenerations following Lesions of the Cerebral Cortex. J Physiol 11: 399-400.

Sokoloff L (1961) Local cerebral circulation at rest and during altered cerebral activity induced by anesthesia or visual stimulation. Regional Neurochemistry: 107-117.

Song SK, Yoshino J, Le TQ, Lin SJ, Sun SW, Cross AH, Armstrong RC (2005) Demyelination increases radial diffusivity in corpus callosum of mouse brain. Neuroimage 26: 132-140.

Sorensen AG, Buonanno FS, Gonzalez RG, Schwamm LH, Lev MH, Huang-Hellinger FR, Reese TG, Weisskoff RM, Davis TL, Suwanwela N, Can U, Moreira JA, Copen WA, Look RB, Finklestein SP, Rosen BR, Koroshetz WJ (1996) Hyperacute stroke: evaluation with combined multisection diffusion-weighted and hemodynamically weighted echo-planar MR imaging. Radiology 199: 391-401.

Spilt A, Box FM, van der Geest RJ, Reiber JH, Kunz P, Kamper AM, Blauw GJ, van Buchem MA (2002) Reproducibility of total cerebral blood flow measurements using phase contrast magnetic resonance imaging. J Magn Reson Imaging 16: 1-5.

Strandgaard S, Paulson OB (1992) Regulation of cerebral blood flow in health and disease. J Cardiovasc Pharmacol 19 Suppl 6: S89-93.

Theberge J (2008) Perfusion magnetic resonance imaging in psychiatry. Top Magn Reson Imaging 19: 111-130.

Trampel R, Jochimsen TH, Mildner T, Norris DG, Moller HE (2004) Efficiency of flow-driven adiabatic spin inversion under realistic experimental conditions: a computer simulation. Magn Reson Med 51: 1187-1193.

Tzourio-Mazoyer N, Landeau B, Papathanassiou D, Crivello F, Etard O, Delcroix N, Mazoyer B, Joliot M (2002) Automated anatomical labeling of activations in SPM using a macroscopic anatomical parcellation of the MNI MRI single-subject brain. Neuroimage 15: 273-289.

van Gelderen P, de Zwart JA, Duyn JH (2008) Pittfalls of MRI measurement of white matter perfusion based on arterial spin labeling. Magn Reson Med 59: 788-795.

van Osch MJ, Teeuwisse WM, van Walderveen MA, Hendrikse J, Kies DA, van Buchem MA (2009) Can arterial spin labeling detect white matter perfusion signal? Magn Reson Med 62: 165-173.

Vonken EJ, van Osch MJ, Bakker CJ, Viergever MA (1999) Measurement of cerebral perfusion with dual-echo multi-slice quantitative dynamic susceptibility contrast MRI. J Magn Reson Imaging 10: 109-117.

Wakana S, Caprihan A, Panzenboeck MM, Fallon JH, Perry M, Gollub RL, Hua K, Zhang J, Jiang H, Dubey P, Blitz A, van Zijl P, Mori S (2007) Reproducibility of quantitative tractography methods applied to cerebral white matter. Neuroimage 36: 630-644.

Wang J, Zhang Y, Wolf RL, Roc AC, Alsop DC, Detre JA (2005) Amplitude-modulated continuous arterial spin-labeling 3.0-T perfusion MR imaging with a single coil: feasibility study. Radiology 235: 218-228.

Weinmann HJ, Brasch RC, Press WR, Wesbey GE (1984) Characteristics of gadolinium-DTPA complex: a potential NMR contrast agent. AJR Am J Roentgenol 142: 619-624.

Weiss JS, Sumpio BE (2006) Review of prevalence and outcome of vascular disease in patients with diabetes mellitus. Eur J Vasc Endovasc Surg 31: 143-150.

Werner R, Norris DG, Alfke K, Mehdorn HM, Jansen O (2005) Improving the amplitude-modulated control experiment for multislice continuous arterial spin labeling. Magn Reson Med 53: 1096-1102.

Wikipedia (2009) In.

Williams DS, Detre JA, Leigh JS, Koretsky AP (1992) Magnetic resonance imaging of perfusion using spin inversion of arterial water. Proc Natl Acad Sci U S A 89: 212-216.

Wolff SD, Balaban RS (1989) Magnetization transfer contrast (MTC) and tissue water proton relaxation in vivo. Magn Reson Med 10: 135-144.

Wong EC (2007) Vessel-encoded arterial spin-labeling using pseudocontinuous tagging. Magn Reson Med 58: 1086-1091.

Wong EC, Buxton RB, Frank LR (1997) Implementation of quantitative perfusion imaging techniques for functional brain mapping using pulsed arterial spin labeling. NMR Biomed 10: 237-249.

Wong EC, Buxton RB, Frank LR (1998) A theoretical and experimental comparison of continuous and pulsed arterial spin labeling techniques for quantitative perfusion imaging. Magn Reson Med 40: 348-355.

Wu WC, Fernandez-Seara M, Detre JA, Wehrli FW, Wang J (2007) A theoretical and experimental investigation of the tagging efficiency of pseudocontinuous arterial spin labeling. Magn Reson Med 58: 1020-1027.

Yang Y, Frank JA, Hou L, Ye FQ, McLaughlin AC, Duyn JH (1998) Multislice imaging of quantitative cerebral perfusion with pulsed arterial spin labeling. Magn Reson Med 39: 825-832.

Ye FQ, Berman KF, Ellmore T, Esposito G, van Horn JD, Yang Y, Duyn J, Smith AM, Frank JA, Weinberger DR, McLaughlin AC (2000) H(2)(15)O PET validation of steady-state arterial spin tagging cerebral blood flow measurements in humans. Magn Reson Med 44: 450-456.